

Correlated Terahertz phonon-ion interactions dominate ion conduction in solid electrolyte $\text{Li}_{0.5}\text{La}_{0.5}\text{TiO}_3$

Kim H. Pham¹, Kiarash Gordiz², Jonathan M. Michelsen¹, Hanzhe Liu¹, Daniele Vivona², Yang Shao-Horn^{2,3}, Asegun Henry², Kimberly A. See^{1*}, Scott K. Cushing^{1*}

Ionic conduction in solids that exceeds 0.01 S/cm is predicted to involve collective phonon-ion interactions in the crystal lattice. Here, we use theory and experiment to measure the contribution of possible collective phonon-ion modes to Li^+ migration in $\text{Li}_{0.5}\text{La}_{0.5}\text{TiO}_3$. The *ab initio* calculations reveal that only a few phonon modes, mostly TiO_6 rocking modes below 6 Terahertz, provide over 40% of the energy required for the Li^+ hop in $\text{Li}_{0.5}\text{La}_{0.5}\text{TiO}_3$. Laser-driving the TiO_6 rocking modes decreases the measured impedance ten-fold compared to exciting acoustic and optical phonons at similar energy densities. The decreased impedance persists on thermalization timescales. These findings provide new insights on phonon-coupled ion migration mechanisms, material design rules, and the potential for metastable states for opto-ionic materials.

Introduction

Solid-state ion conduction has applications in Li-ion batteries¹, biological membranes², solid oxide fuel cells³, and more. Ongoing research in this field has led to the continual improvement of superionic conductors that can enable energy dense solid-state electrochemical systems while maintaining fast conductive properties akin to liquids^{4–8}. Realizing an all-solid-state battery with a superionic solid-state electrolyte and a Li metal anode can meet the necessary energy and power requirements for developing electric, long-range vehicles, and improve safety⁹.

The fundamental mechanism of ion conduction (σ_{ion}) relies on the Arrhenius form equation as shown in **Eq. 1**, where σ_0 is the Arrhenius pre-factor, T is temperature, E_a is the activation energy, and k_B is the Boltzmann constant¹⁰.

$$\sigma_{ion} = \frac{\sigma_0}{T} * \exp\left(-\frac{E_a}{k_B T}\right) \quad 1$$

Researchers have sought out different strategies to increase σ_{ion} by lowering the E_a of the ion migration pathway via targeting lattice structures with corner sharing frameworks⁶ and connected migration channels^{9,11}, employing highly polarizable polyanions in the sub-lattice^{12,13}, introducing disorder to cation sites^{6,8}, and leveraging polyanion-motion-mediated ion transport^{14–16}. These principles have led to the discovery of several superionic conductors through aliovalent/isovalent substitution strategies¹⁷ and a general search for ideal structural families^{8,13,14,16}. $\text{Li}_{10}\text{GeP}_2\text{S}_{12}$ ^{4,6,7}, $\text{Li}_7\text{P}_3\text{S}_{11}$ ^{6,9,14,15}, and

Li -argyrodites^{6,8,12} are extraordinarily conductive, but the exact mechanisms supporting superionic conductivity remain debated. In particular, coupling of phonon-ion vibrations have been suggested to play a significant role in the ion conduction mechanism^{13,18–21}.

To understand phonon-ion coupling, we can expand the pre-factor σ_0 in **Eq. 1**. As shown in **Eq. 2**, σ_{ion} depends on the entropy of migration (ΔS_m) and enthalpy of migration (ΔH_m)¹³.

$$\sigma_{ion} \propto \exp\left(\frac{\Delta S_m}{k_B}\right) \exp\left(-\frac{\Delta H_m}{k_B T}\right) * \frac{1}{T} \quad 2$$

The value of ΔS_m is determined by collective phonon-ion interactions²², which are predicted to correlate with and enhance ionic conductivity^{13–24}. The value of ΔH_m is experimentally measured as the E_a (determined by **Eq. 1**).

Several experimental efforts have attempted to explore the phonon-ion couplings predicted to relate to ΔS_m . Nuclear Magnetic Resonance (NMR) techniques have been used to probe phonon-ion coupling in Li-argyrodites^{18,25} and other conductive Li-sulfide, -nitride, and -oxides²⁶. Neutron scattering techniques have been applied to Na-sulfides and -selenides^{16,19}, as well as Na-orthophosphates and -sulphates^{16,27}, specifically by characterizing the reorientation of anions as quasi-elastic structure factors^{26,27}.

Another approach to measure the role of different phonon-ion couplings is to drive relevant modes with light and measure the resulting effect on conductivity. The THz region, in particular, can

¹Division of Chemistry and Chemical Engineering, California Institute of Technology, Pasadena, CA, USA. ²Department of Mechanical Engineering, Massachusetts Institute of Technology, Cambridge, MA, USA. ³Research Laboratory of Electronics, Massachusetts Institute of Technology, Cambridge, MA, USA. *Correspondence to: ksee@caltech.edu, scushing@caltech.edu

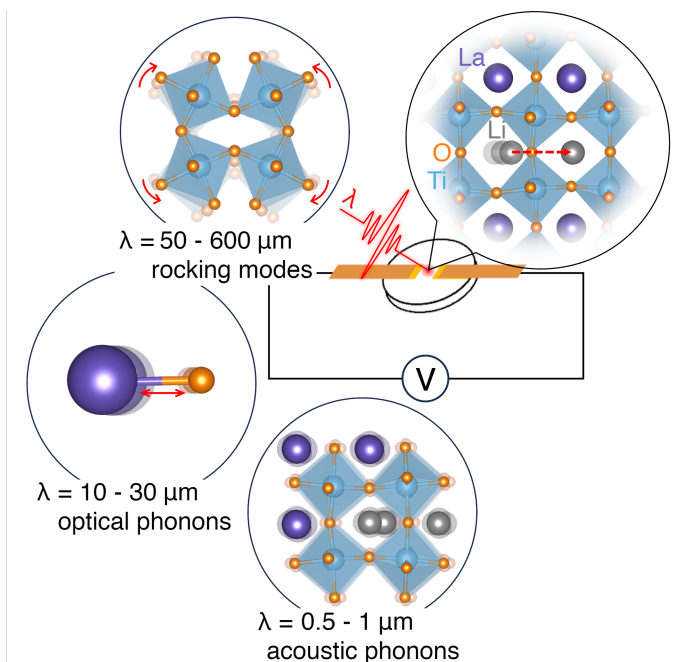


Fig. 1 | Schematic of the laser-driven impedance method with LLTO. An excitation source (λ) excites the sample between two in-plane Au electrodes while EIS measurements are collected. Depending on the wavelength of the excitation source, rocking modes, optical phonons, and acoustic phonons can be excited to influence the Li^+ migration in LLTO.

selectively target polyanion modes theorized to mediate ion transport^{24,28–31}. Specifically, modes that involve $(\text{PS}_4^{3-})^{14,19}$, $(\text{SiS}_4^{4-})^{14}$, $(\text{PO}_4^{3-})^{31}$, $(\text{YBr}_6^{3-})^{32}$, and $(\text{ErCl}_6^{3-})^{32}$ polyanion vibrations all fall within the low THz frequencies^{18,24,31,32}—equivalent to picosecond hopping timescales¹⁶. The same modes are theorized to be responsible for coupled hopping in LISICON-like conductors ($\text{Li}_{10}\text{SiP}_2\text{S}_{12}$ ³³, LGPS^{4,24}, Li_3PO_4 ^{21,31}, LPS^{14,24}), Li-argyrodites ($\text{Li}_6\text{PS}_5\text{Cl}$, $\text{Li}_6\text{PS}_5\text{Br}$)^{12,18}, and superionic Li-halides (Li_3YBr_6 , Li_3ErCl_6)^{24,32}. Similarly, octahedral rotations are also reported to promote fast ionic transport in several perovskite-related phases^{20,34,35}, making phonon-driven ionics widely applicable for understanding phonon-ion coupling in many known superionic conductors.

While driving acoustic and optical modes to change electronic and magnetic properties is common in condensed matter physics^{23,36,37}, very few studies directly drive phonon-ion couplings to promote ion transport^{28,29}. In one report, Poletayev *et al.* employed a THz pump to induce a Na^+ , K^+ , and Ag^+ ion hop in $\beta\text{-Al}_2\text{O}_3$ and then measured the change in birefringence using an 800 nm probe. The THz Kerr Effect measured the anisotropy caused by

an ion hop, which they calculate to lead to a 20x increase in hop anisotropy compared to thermal conditions²⁹. In addition, Gordiz *et al.* used Nudged-Elastic Band (NEB) calculations and Molecular Dynamic (MD) simulations to predict that over 87% of the lattice energy required for the ion hop in Ge-substituted Li_3PO_4 came from <10% of the modes in the system³¹. By computationally exciting highly contributing modes, they enhanced the ionic conductivity by orders of magnitude without increasing the bulk temperature.

In this paper, we use *ab initio* calculations, MD simulations, and experiments that combine laser driving and EIS to determine the role of octahedral rocking TiO_6 modes on the hopping of Li^+ in $\text{La}_{0.5}\text{Li}_{0.5}\text{TiO}_3$ (LLTO). The bottleneck of Li^+ migration in LLTO (**Fig. S17**) comprises 4 oxygen atoms formed by 4 corner sharing TiO_6 octahedra^{34,35} that are reported to “rock” in place at low THz frequencies. To determine the contribution of rocking TiO_6 modes on Li^+ migration, we excite those modes with THz irradiation from 0.5 to 6 THz, or 50 - 600 μm (general schematic shown in **Fig. 1**). The La-O mode (11.6 μm) is predicted to weaken if Li^+ interactions with the TiO_6 octahedra are strong³⁵, so we next test whether driving the La-O vibrations with MIR light (9.4 - 14.16 μm) can weaken Li^+ - TiO_6 -coupling and modulate Li^+ transport. Finally, to compare the effect of exciting random thermal vibrations versus selective phonon driving on ion transport and to confirm the nature of the metastability³¹, we drive acoustic phonon modes with NIR light (800 nm or 0.8 μm) and with DC heating. We use EIS to probe the subsequent decrease in impedance due to NIR – THz excitation which should correlate with ion transport behavior.

Experimentally, we find that the final percent change in $R_{\text{bulk}}/\text{mW}$ from THz excitation is 0.68% per mW, approximately 6x the change caused by 800 nm light or optical heating (0.12 % per mW) and nearly 10x the change caused by thermal heating (0.07% per mW) before temperature normalization (**Table S2**). Upon removal of the excitation sources, the relaxation to the initial impedance occurs on the same timescale as sample thermalization. The exhibited metastability and magnitude of enhancement suggests an initial, impulsive change to unique non-equilibrium ion distributions that depends on the excitation energy.

We therefore quantify the enhancement at steady-state. We normalize the measured enhancement by change in sample temperature (see

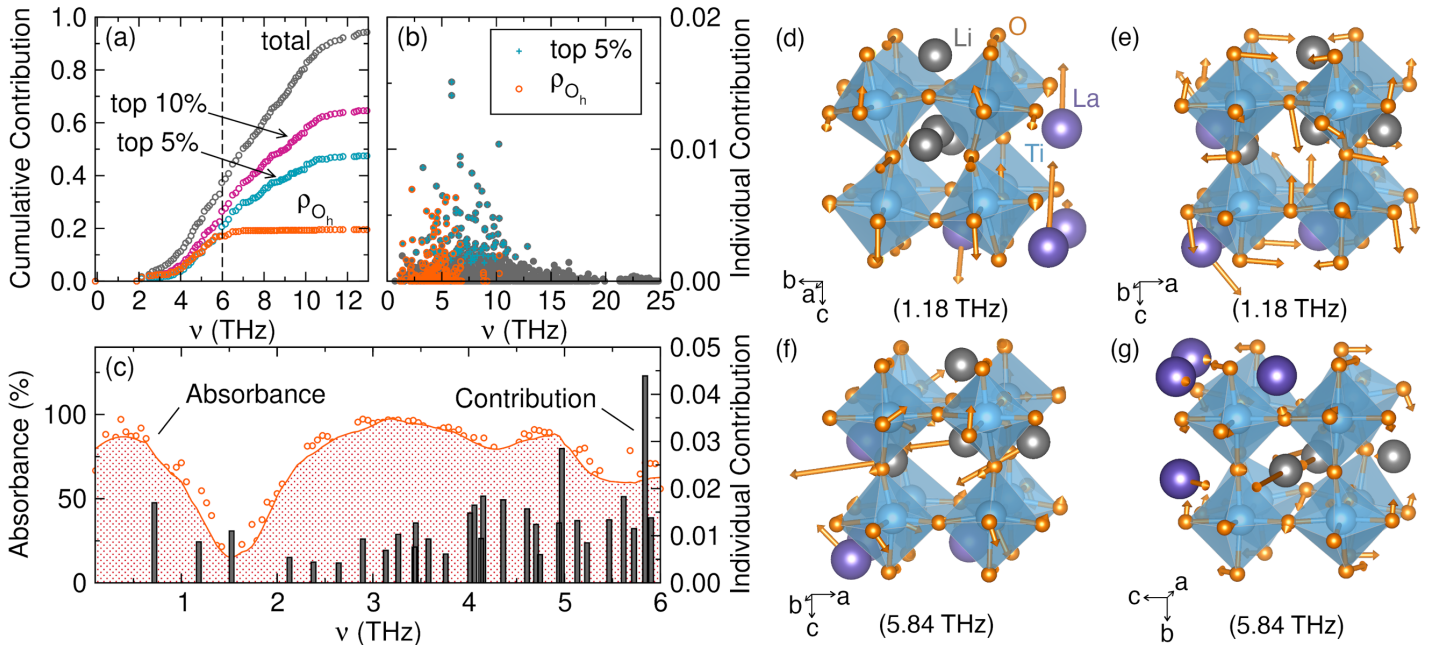


Fig. 2 | Calculated phonon contributions to Li^+ hopping, THz absorbance, and representative LLTO phonon modes. **a**, the cumulative contributions of phonon modes to the normalized energy required for ion hopping, and **b**, the individualized contributions of phonon modes to the normalized energy required for ion hopping where ρ_{O_h} represents octahedral rocking modes. The data is normalized over all 22 Li^+ hop investigations). The black line in **a** indicates the experimental limit in THz generation (6 THz). **c**, LLTO THz absorbance (orange) versus calculated phonon contribution to Li^+ hop (bar graph). **d-g**, representation of calculated phonon mode contributions, where **d** and **e** represent modes that are not coupled to ion hopping because they have no vibrational eigenvectors on the Li^+ sublattice, and **f** and **g** represent modes that are.

Fig. S10-S12 and **Table S2-S3** for details) to compare enhancements across different excitation energies. Given that the change in impedance at steady state is similar between laser heating (NIR) and DC heating, the relative enhancement from laser excitation reflects the impact of each mode on thermal ion transport. We compare the measured changes in impedance against theory for ion transport in the thermal state to further verify the measured phonon mode effects on ion migration.

In agreement with the *ab initio* calculations, our measurements confirm that selectively exciting the THz rocking modes leads to an order of magnitude decrease in the bulk and grain boundary resistance, or R_{bulk} and R_{gb} , as compared to exciting acoustic or optical modes, likely due to coupling between the TiO_6 and hopping Li^+ . Reminiscent of other metastable phases induced by light in inorganic-organic hybrid perovskites³⁸⁻⁴¹,—the enhancement that we measured is persistent and reversible, even though the recorded changes are averaged over the 1 kHz modulation rate provided by the laser. Our results intriguingly suggest that laser driving specific phonon modes can facilitate fast ion transport in a solid and can inform new design principles to achieve ionic conductivities greater

than 1 mS/cm. Our results motivate future work in picosecond temporal impedance measurements to further explore the dynamics of ion hopping and the observed metastability.

Results

Using *ab initio* calculations, the contributions of vibrational modes to the energy needed by Li^+ to reach its transition state (herein referred to as ion hopping) in LLTO were calculated based on the magnitude of the projection of the atomic displacement field obtained for the transition state on the eigenvectors of vibration for each specific phonon, as explained in detail in **Section S13**. The structure parameters for the calculations were obtained from quantitative Rietveld refinements of experimental synchrotron diffraction data (**Fig. S1**). To efficiently sample different possible Li^+ ion hops and relevant contributing vibrational modes, 22 unique Li^+ hops based on two different hopping mechanisms (single and concerted) across three degrees of La | Li disorder in the LLTO lattice were chosen and analyzed (**Fig. S15**).

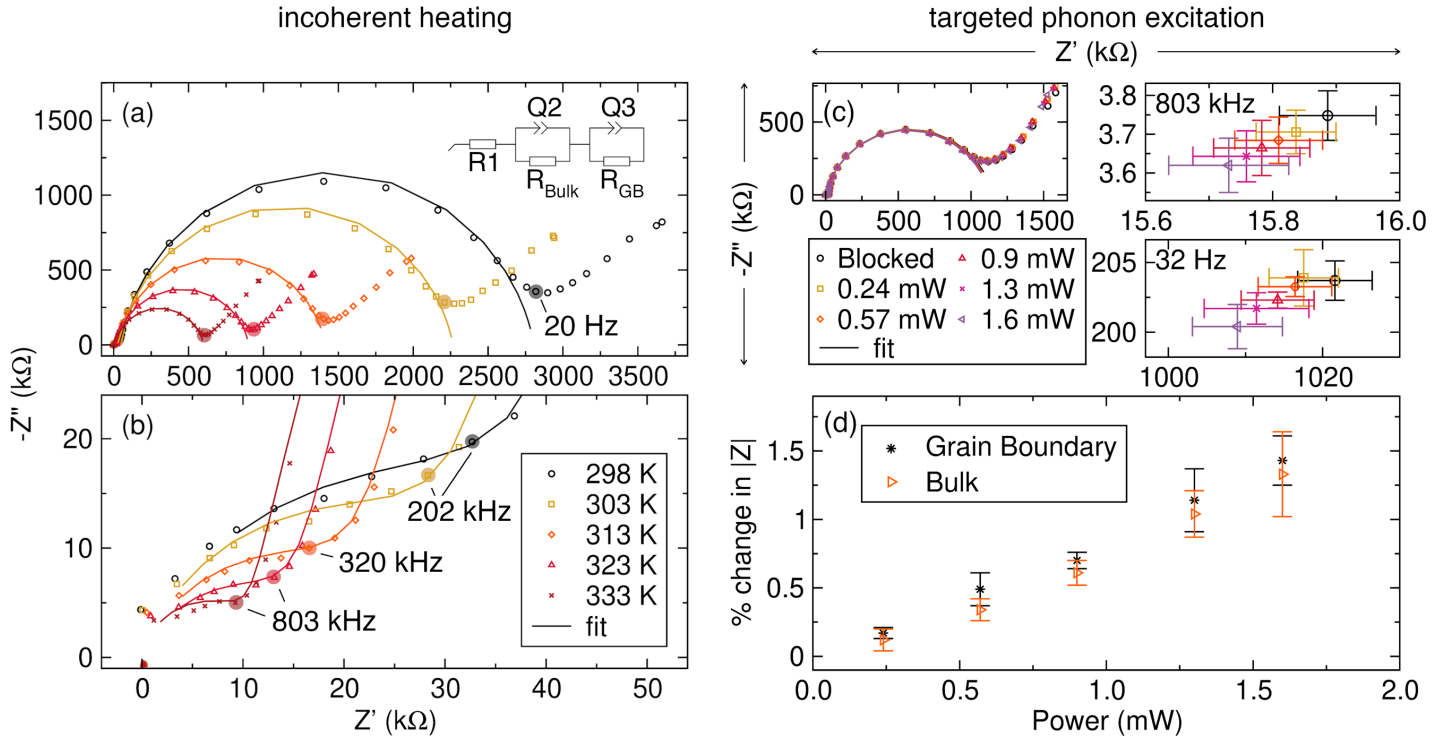


Fig. 3 | Nyquist plots of LLTO between 298 K-333 K and from targeted phonon excitation with THz. Nyquist plots focused on the **a**, grain boundary feature, and **b**, bulk feature, of LLTO. The symbols correspond to the data and the line represents the fit to the equivalent circuit shown in **a**. **c**, Nyquist plots of LLTO with 0-1.6 mW of THz excitation at various powers. See SI for fitting details. The change in Z' is compared at 803 kHz and 32 Hz, corresponding to bulk and grain boundary resistance, respectively. **d**, The percent change in impedance versus power after illumination. The linearity of these data rules out non-linear effects from the THz driving field.

Fig. 2a shows the normalized cumulative contribution of different phonon modes to the Li^+ hopping process, here defined as the energy needed for a Li^+ to reach its transition state. **Fig. 2b** shows the individual breakdown of the total phonon mode contributions that sum to **Fig. 2a**. Rocking modes are distinguished in both panels. Experimentally, the phonon modes were only excited up to the instrument limit of 6 THz. The THz absorbance spectrum of LLTO and the theoretical contributing mode density is shown in **Fig. 2c**. Thus, we narrow our further discussion of the *ab initio* calculations and MD simulations to this region.

The phonon modes below 6 THz contribute to over 40% of all ion hops sampled, as shown in **Fig. 2a** as the frequencies lower than the dashed line, corroborating that low frequency phonon modes strongly influence ion transport as studied in other theoretical reports^{15,24}.

Although some non-rocking type modes do not contribute to hopping shown in **Fig. 2d** and **2e**, we find that the majority of highly contributing THz phonon modes are collective rocking modes represented in **Fig. 2f** and **2g**. Thus, to effectively promote ion transport, the surrounding polyhedra

must collectively transfer sufficient energy to the Li^+ along the hopping direction to promote an ion hop. The significance of this contribution is further supported by the increase in ion hopping rate observed in MD simulations (see **Section S18** and **Table S4**). Due to the low frequency nature of modes below 6 THz, the inclusion of quantum effects changes their contribution by less than 1% (see **Fig. S19** and **Section S17**), making the calculations relevant to the room temperature experiments.

To experimentally test the predicted contributions of rocking modes (see **Fig. S18** and **Section S16**) to Li^+ hopping, LLTO is first synthesized in accordance with literature⁴² and structurally characterized (see **Section S1-S2**). We then irradiated the LLTO up to 6 THz (bandwidth set by the generation process) and then measured the perturbation on the R_{bulk} and R_{GB} determined from fitting Nyquist plots measured by EIS.

Before conducting the laser-driven impedance measurement, we perform variable-temperature EIS measurements as a control (see **Section S3-S7**). The Nyquist plots for LLTO with no laser excitation are shown in **Fig. 3a** and **3b**. Since the sample geometry has irregular (i.e. nonplanar)

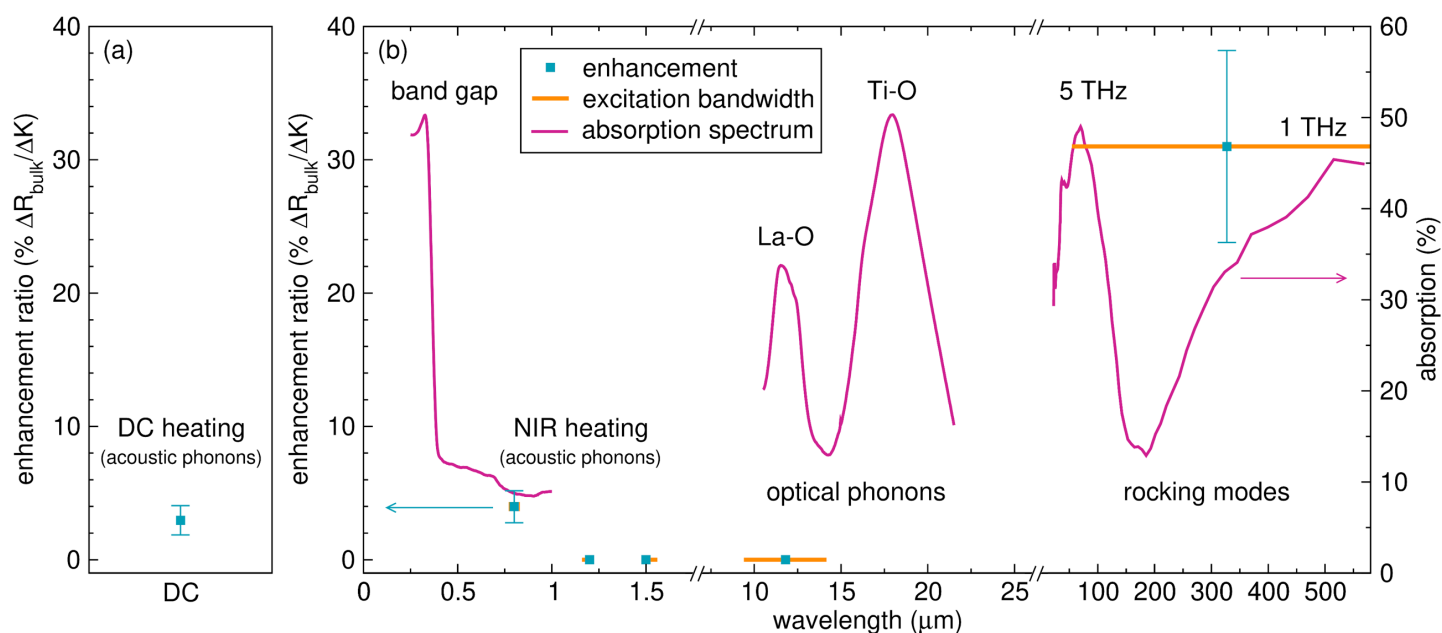


Fig. 4 | Enhancement in bulk ion migration due to illumination across DC heating, near-IR (NIR), mid-IR (MIR), and THz light. **a**, the enhancement ratio calculated from heating LLTO between 298 K to 333 K shown as percent change in R_{bulk} per change in sample temperature (K). The DC heating corresponds to incoherent heating of the acoustic phonon bath. **b**, enhancement ratios (cyan squares) calculated from exciting LLTO between NIR – THz light overlaid with the absorption spectrum of LLTO from NIR – THz (purple). The width of the horizontal orange bar represents the spectral width of the excitation pulse. The NIR enhancement corresponds to incoherent heating of the acoustic phonon bath. The MIR excitation corresponds to coherent driving of optical phonon modes, which was inconclusive for the same excitation density as the THz modes. The THz light coherently drives highly contributing modes, showing the largest relative enhancement.

surfaces with no accurately defined thickness, the ionic conductivity cannot be calculated. R_{bulk} and R_{GB} is used instead to study the changes in ion migration due to NIR- THz excitation. The impedance data for the bulk feature (**Fig. 3a**) and grain boundary feature (**Fig. 3b**) impedance were fit to the $R1+R_{\text{bulk}}/Q2+R_{\text{GB}}/Q3$ circuit shown in **Fig. 3a**. As temperature increases, the impedance decreases for Z' and Z'' because of the increase in population and mode types in the phonon bath, in agreement with **Eq. 1**. The semi-circle fit corresponding to the grain boundary contribution (**Fig. 3b**) has a different shape than the bulk contribution (**Fig. 3a**), likely because the bulk semi-circle partially overlaps with the grain boundary feature, and that the grain boundary feature is characterized by irregular surfaces. The change in impedance is linear with temperature within error (**Fig. S12**).

EIS measurements are then repeated while driving the THz phonon modes with 0.1-1 mW of THz power focused to a 250 μm beam diameter using an open electrochemical cell (**Section S2 and S4**). When the 0.5 – 6 THz modes are driven, a linear decrease in the Z' on the order of 100s of Ω is

measured with increasing power for both the bulk and grain boundary features (**Fig. 3c-d**). The change is reversible, reverting to the pre-irradiated impedance after irradiation (**Fig. S6**). EIS measurements under irradiation were next repeated with MIR and NIR light (**Section S5**). MIR light was used to probe the La-O mode at 11.6 μm , with a 0.1 mW average power focused to a 250 μm beam diameter. The acoustic phonon modes were driven with up to 25 mW of 800 nm light focused into a 250 μm beam diameter.

Since we measure the thermally averaged state, we normalize all changes in impedance for each excitation frequency by change in sample temperature, as shown in **Fig. 4** and determined with a calibration curve shown in **Fig. S11**. The normalization accounts for the different absorption cross sections for the different vibrational mode regions (**Eq. 1-2**), although trends are the same when normalized by power density (**Table S2 and S3**). The normalized change for incoherent laser heating and DC heating gives similar values within error (3-4% $\Delta R_{\text{bulk}}/K$) and should be taken as the baseline for the experiments (**Fig. 4a and 4b** respectively). Any

normalized change in impedance above this value reflects a non-thermal increase in conductivity.

With the THz light, a 31% change in $\Delta R_{\text{bulk}}/\Delta K$ is calculated. Incoherently heating the acoustic phonon bath with the 800 nm light gives a calculated 4% change in $\Delta R_{\text{bulk}}/\Delta K$. This change is comparable to the 3% change in $\Delta R_{\text{bulk}}/\Delta K$ from DC heating, within error, proving that laser heating of the lattice alone is not responsible for the observed changes caused by THz light. No detectable change is measured between 9.4 – 14.16 μm for the same power densities used to drive the THz phonon modes. The MIR power is 100x lower than the power needed for incoherent laser-induced thermal heating, so the relative role can only be bound by these ranges. The result is consistent with our theoretical calculations where the optical modes contribute significantly less to ion hopping above 10 THz ($\sim 30 \mu\text{m}$) shown in **Fig. 2b**, which possibly justify why no detectable changes are observed.

Discussion

The relative decrease in R_{bulk} with THz light is ten-fold that compared to incoherent DC heating, experimentally confirming that the theoretically predicted phonon-ion coupled modes do promote ion migration at higher rates than uncorrelated thermal, acoustic phonon induced hops. Also, any electronic contribution toward the total measured impedance, or any excitation of electronic carriers due to THz fields, are unlikely in LLTO because no change to the open circuit voltage is measured. Further, the THz radiation is $<0.025 \text{ eV}^{43}$, which is sufficiently below the 2.1 eV band gap of LLTO⁴⁴, and no nonlinear effects are observed. Therefore, it is unlikely that the THz fields can generate electronic carriers or have sufficient energies to promote enhanced electronic conductivities seen in other material known to exhibit smaller energy-gap transitions³⁷.

The timescale of the thermal relaxation from the 800 nm excitation matches that of the THz when the change in impedance reaches a steady state (**Fig. S6 and S7**). The THz modes, after excitation, ultimately decay into the same incoherent phonon bath as the induced incoherent heating with 800 nm light, explaining the similar decay timescales measured in the steady state (**Fig. S6 and S7**). Upon removal of the THz excitation, the non-equilibrium ion hopping state that is induced is then reversed on the timescale of the slower, thermalized acoustic phonon bath. The time resolution of our EIS

measurements (milliseconds) prevents direct measurement of the “peak” enhancement by the laser and only the end thermalization, but future work can measure the ultrafast timescales ($< \text{ns}$) necessary to explore the nature of the excited, perturbed state. Additionally, when the change in impedance is normalized by change in sample temperature, a heating effect alone does not explain the differences in enhancement that we measure between the THz and DC heating or the incoherent laser heating with 800 nm (**Fig. 4**).

We hypothesize that the THz-induced metastable state is first generated upon impulsive excitation. Optically induced metastable states have been generated experimentally by resonantly photoexciting solid-state materials which can modify lattice strain, magnetism, polar states, and ferroelectric states^{38,39}. Non-equilibrium phases can also be generated by THz driving and may explain the difference in steady-state impedance change, but such conclusions cannot be confidently drawn without developing ultrafast impedance probes⁴⁵.

In conclusion, we compare the relative role of acoustic, optical, and phonon modes in ion migration through laser-frequency-selective perturbation of EIS measurements. For example, by directly driving highly contributing phonon modes, which are most likely rocking modes in the 0.5-6 THz region, a ten-fold enhancement in ion migration is measured relative to incoherent heating. The significant contribution of rocking modes to ion hopping in the $<6 \text{ THz}$ region agrees with *ab initio* calculations, validating its use in exploring phonon mediated hopping and confirming that only a small percentage of phonon mode types lead to the majority of ion migration. The findings herein can aid in the design of future solid-state ion conductors. The results also hint at the potential for exploring metastable light-induced states for ionic transport that could lead to new applications and sciences that require new ultrafast spectroscopy techniques.

References:

1. Song, S., Hu, N. & Lu, L. Solid electrolytes for solid-state Li/Na–metal batteries: inorganic, composite and polymeric materials. *Chem. Commun.* **58**, 12035–12045 (2022).
2. Mei, T., Zhang, H. & Xiao, K. Bioinspired Artificial Ion Pumps. *ACS Nano* **16**, 13323–13338 (2022).
3. Sun, S. *et al.* A focused review on structures and ionic conduction mechanisms in inorganic

- solid-state proton and hydride anion conductors. *Mater. Adv.* **4**, 389–407 (2023).
- Bhandari, A. & Bhattacharya, J. Origin of Fast Ion Conduction in $\text{Li}_{10}\text{GeP}_2\text{S}_{12}$, a Superionic Conductor. *J. Phys. Chem. C* **120**, 29002–29010 (2016).
 - Choi, Y.-S. & Lee, J.-C. Electronic and mechanistic origins of the superionic conductivity of sulfide-based solid electrolytes. *Journal of Power Sources* **415**, 189–196 (2019).
 - Jun, K. *et al.* Lithium superionic conductors with corner-sharing frameworks. *Nat. Mater.* **21**, 924–931 (2022).
 - Kamaya, N. *et al.* A lithium superionic conductor. *Nature Mater* **10**, 682–686 (2011).
 - Kraft, M. A. *et al.* Inducing High Ionic Conductivity in the Lithium Superionic Argyrodites $\text{Li}_{6+x}\text{P}_{1-x}\text{Ge}_x\text{S}_5\text{I}$ for All-Solid-State Batteries. *J. Am. Chem. Soc.* **140**, 16330–16339 (2018).
 - Manthiram, A., Yu, X. & Wang, S. Lithium battery chemistries enabled by solid-state electrolytes. *Nat Rev Mater* **2**, 1–16 (2017).
 - Goodenough, J. B. Review Lecture - Fast ionic conduction in solid. *Proceedings of the Royal Society of London. A. Mathematical and Physical Sciences* **393**, 215–234 (1997).
 - Weber, D. A. *et al.* Structural Insights and 3D Diffusion Pathways within the Lithium Superionic Conductor $\text{Li}_{10}\text{GeP}_2\text{S}_{12}$. *Chem. Mater.* **28**, 5905–5915 (2016).
 - Kraft, M. A. *et al.* Influence of Lattice Polarizability on the Ionic Conductivity in the Lithium Superionic Argyrodites $\text{Li}_6\text{PS}_5\text{X}$ (X = Cl, Br, I). *J. Am. Chem. Soc.* **139**, 10909–10918 (2017).
 - Muy, S., Schlem, R., Shao-Horn, Y. & Zeier, W. G. Phonon–Ion Interactions: Designing Ion Mobility Based on Lattice Dynamics. *Advanced Energy Materials* **11**, 2002787 (2021).
 - Zhang, Z. *et al.* Targeting Superionic Conductivity by Turning on Anion Rotation at Room Temperature in Fast Ion Conductors. *Matter* **2**, 1667–1684 (2020).
 - Smith, J. G. & Siegel, D. J. Low-temperature paddlewheel effect in glassy solid electrolytes. *Nat Commun* **11**, 1483 (2020).
 - Zhang, Z. & Nazar, L. F. Exploiting the paddlewheel mechanism for the design of fast ion conductors. *Nat Rev Mater* **7**, 389–405 (2022).
 - Bachman, J. C. *et al.* Inorganic Solid-State Electrolytes for Lithium Batteries: Mechanisms and Properties Governing Ion Conduction. *Chem. Rev.* **116**, 140–162 (2016).
 - Hanghofer, I., Gadermaier, B. & Wilkening, H. M. R. Fast Rotational Dynamics in Argyrodite-Type $\text{Li}_6\text{PS}_5\text{X}$ (X: Cl, Br, I) as Seen by ^{31}P Nuclear Magnetic Relaxation—On Cation–Anion Coupled Transport in Thiophosphates. *Chem. Mater.* **31**, 4591–4597 (2019).
 - Krauskopf, T. *et al.* Comparing the Descriptors for Investigating the Influence of Lattice Dynamics on Ionic Transport Using the Superionic Conductor $\text{Na}_3\text{PS}_{4-x}\text{Se}_x$. *J. Am. Chem. Soc.* **140**, 14464–14473 (2018).
 - Li, X. & Benedek, N. A. Enhancement of Ionic Transport in Complex Oxides through Soft Lattice Modes and Epitaxial Strain. *Chem. Mater.* **27**, 2647–2652 (2015).
 - Muy, S. *et al.* Tuning mobility and stability of lithium ion conductors based on lattice dynamics. *Energy Environ. Sci.* **11**, 850–859 (2018).
 - Vineyard, G. H. Frequency factors and isotope effects in solid state rate processes. *Journal of Physics and Chemistry of Solids* **3**, 121–127 (1957).
 - Först, M. *et al.* Nonlinear phononics as an ultrafast route to lattice control. *Nature Phys* **7**, 854–856 (2011).
 - Xu, Z., Chen, X., Zhu, H. & Li, X. Anharmonic Cation–Anion Coupling Dynamics Assisted Lithium-Ion Diffusion in Sulfide Solid Electrolytes. *Advanced Materials* **n/a**, 2207411.
 - Brinek, M., Hiebl, C., Hogrefe, K., Hanghofer, I. & Wilkening, H. M. R. Structural Disorder in $\text{Li}_6\text{PS}_5\text{I}$ Speeds ^7Li Nuclear Spin Recovery and Slows Down ^{31}P Relaxation—Implications for Translational and Rotational Jumps as Seen by Nuclear Magnetic Resonance. *J. Phys. Chem. C* **124**, 22934–22940 (2020).
 - Wilkening, M. & Heitjans, P. From Micro to Macro: Access to Long-Range Li^+ Diffusion Parameters in Solids via Microscopic $^6, ^7\text{Li}$ Spin-Alignment Echo NMR Spectroscopy. *ChemPhysChem* **13**, 53–65 (2012).
 - Wilmer, D., Feldmann, H., Lechner, R. E. & Combet, J. Sodium Ion Conduction in Plastic Phases: Dynamic Coupling of Cations and Anions in the Picosecond Range. *J. Mater. Res.* **20**, 1973–1978 (2005).
 - Morimoto, T. *et al.* Microscopic ion migration in solid electrolytes revealed by terahertz time-

- domain spectroscopy. *Nat Commun* **10**, 2662 (2019).
29. Poletayev, A. D. *et al.* The persistence of memory in ionic conduction probed by nonlinear optics. *Nature* **625**, 691–696 (2024).
 30. Gray, A. X. *et al.* Ultrafast terahertz field control of electronic and structural interactions in vanadium dioxide. *Phys. Rev. B* **98**, 045104 (2018).
 31. Gordiz, K., Muy, S., Zeier, W. G., Shao-Horn, Y. & Henry, A. Enhancement of ion diffusion by targeted phonon excitation. *CR-PHYS-SC* **2**, (2021).
 32. Schlem, R., Banik, A., Ohno, S., Suard, E. & Zeier, W. G. Insights into the Lithium Substructure of Superionic Conductors Li₃YCl₆ and Li₃YBr₆. *Chem. Mater.* **33**, 327–337 (2021).
 33. Zhang, B., Yang, L., Wang, L.-W. & Pan, F. Cooperative transport enabling fast Li-ion diffusion in Thio-LISICON Li₁₀SiP₂S₁₂ solid electrolyte. *Nano Energy* **62**, 844–852 (2019).
 34. Stramare, S., Thangadurai, V. & Weppner, W. Lithium Lanthanum Titanates: A Review. *Chem. Mater.* **15**, 3974–3990 (2003).
 35. Guo, X., Maram, P. S. & Navrotsky, A. A correlation between formation enthalpy and ionic conductivity in perovskite-structured Li_{3x}La_{0.67-x}TiO₃ solid lithium ion conductors. *J. Mater. Chem. A* **5**, 12951–12957 (2017).
 36. Nova, T. F. *et al.* An effective magnetic field from optically driven phonons. *Nature Phys* **13**, 132–136 (2017).
 37. Hu, W. *et al.* Optically enhanced coherent transport in YBa₂Cu₃O_{6.5} by ultrafast redistribution of interlayer coupling. *Nature Mater* **13**, 705–711 (2014).
 38. Nova, T. F., Disa, A. S., Fechner, M. & Cavalleri, A. Metastable ferroelectricity in optically strained SrTiO₃. *Science* **364**, 1075–1079 (2019).
 39. Frank Y. Gao *et al.* Snapshots of a light-induced metastable hidden phase driven by the collapse of charge order | Science Advances. <https://www.science.org/doi/10.1126/sciadv.abp9076>.
 40. Chen, Z., Brocks, G., Tao, S. & Bobbert, P. A. Unified theory for light-induced halide segregation in mixed halide perovskites. *Nat Commun* **12**, 2687 (2021).
 41. Draguta, S. *et al.* Rationalizing the light-induced phase separation of mixed halide organic–inorganic perovskites. *Nat Commun* **8**, 200 (2017).
 42. Fourquet, J. L., Duroy, H. & Crosnier-Lopez, M. P. Structural and Microstructural Studies of the Series La_{2/3-x}Li_{3x}□_{1/3-2x}TiO₃. *Journal of Solid State Chemistry* **127**, 283–294 (1996).
 43. Greene, B. I., Saeta, P. N., Dykaar, D. R., Schmitt-Rink, S. & Chuang, S. L. Far-infrared light generation at semiconductor surfaces and its spectroscopic applications. *IEEE Journal of Quantum Electronics* **28**, 2302–2312 (1992).
 44. Zhang, L. *et al.* Lithium lanthanum titanate perovskite as an anode for lithium ion batteries. *Nat Commun* **11**, 3490 (2020).
 45. Liu, B. *et al.* Generation of narrowband, high-intensity, carrier-envelope phase-stable pulses tunable between 4 and 18 THz. *Opt. Lett., OL* **42**, 129–131 (2017).

Acknowledgements

FT-IR data was collected at the Laser Resource Center in the Beckman Institute of the California Institute of Technology with the assistance of Dr. Jay Winkler. Solid-state UV-VIS data was collected at the Earle M. Jorgenson Laboratory of the California Institute of Technology with the assistance of Dr. Weilai Yu. We thank Prof. David Hsieh and Omar Mehio for assistance in using the difference frequency generation unit for IR light. We thank Ricardo Zarazua at the Chemistry and Chemical Engineering Machine Shop for machining the custom heating cell in this work. We thank Zachary W. B. Iton for assistance with SEM data collection in the Supporting Information. Use of the Advanced Photon Source at Argonne National Laboratory was supported by the U. S. Department of Energy, Office of Science, Office of Basic Energy Sciences, under Contract No.DE-AC02-06CH1135.

Funding

Financial support was provided by the National Science Foundation, Air Force Office of Science & Research, and David & Lucile Packard Foundation.

Author Contributions

S.K.C. and K.A.S. supervised the project. S.K.C. and K.A.S. conceived the work. S.K.C., K.A.S., and K.H.P. designed the experiments. K.H.P. conducted the synthesis, developed the laser-driven impedance method, collected, and analyzed the light-induced impedance measurements. J.M.M. and H.L. generated the THz radiation, characterized the THz

spectrum, and supported the integration of THz with the impedance technique. K.G. and D.V. performed the atomistic simulations. K.H.P. and K.G. wrote the manuscript. S.K.C., K.A.S., D.V., A.H., and Y.S.H. edited the manuscript.

Data Availability Statement

All data supporting the findings of this work are available in the Supplementary Information. The computational data that supports the findings of this

study can be obtained from the corresponding author on request.

Code Availability Statement

The code is available under the MIT license and can be found at <https://github.com/kgordiz/modalNEB>.

Ethics Declaration

Competing interests

The authors declare no competing interests

Many-body phonon-ion conduction in solid electrolyte driven by THz modes

Kim H. Pham¹, Kiarash Gordiz², Jonathan M. Michelsen¹, Hanzhe Liu¹, Daniele Vivona², Yang Shao-Horn^{2,3}, Asegun Henry^{2*}, Kimberly A. See^{1*}, Scott K. Cushing^{1*}

¹Division of Chemistry and Chemical Engineering, California Institute of Technology, Pasadena, CA, USA

²Department of Mechanical Engineering, Massachusetts Institute of Technology, Cambridge, MA, USA.

³Research Laboratory of Electronics, Massachusetts Institute of Technology, Cambridge, MA, USA.

*Correspondence to: ase@mit.edu, ksee@caltech.edu, scushing@caltech.edu

Section S1. Synthesis. $\text{Li}_{0.5}\text{La}_{0.5}\text{TiO}_3$ (LLTO) was synthesized according to literature.¹ A stoichiometric amount of La_2O_3 , Li_2CO_3 and TiO_2 were mixed in an agate mortar and pressed into pellets under 100 MPa of pressure. The pellets were placed on a bed of sacrificial powder and calcined at 800 °C for 4 h then 1200 °C for 12 h at a ramp rate of 1 °C / min. The following material was routinely characterized using a Rigaku X-ray diffractometer with $\text{CuK}\alpha$ radiation and scanned from 10 to 80 2θ at a scan rate of 0.4° per second. The following x-ray diffraction pattern was fitted using a Rietveld refinement with the GSAS II software. High resolution synchrotron powder diffraction data were collected using beamline 11-BM at the Advanced Photon Source (APS), Argonne National Laboratory. Scanning electron microscopy was taken (a) looking down the cross-section, and (b) on the surface of an annealed LLTO pellet. SEM was performed using the SE2 detector of a ZEISS 1550VP field emission SEM with an acceleration voltage of 10 kV at 10xK magnification.

Section S2. Sample Preparation. The resulting powder was pressed into a pellet with a diameter of 9 mm and a thickness of 0.7 mm under 2 tons of pressure, yielding a 75-76% pellet density. The pellet was subsequently annealed at 1100 °C for 6 h at a ramp rate of 2 °C / min over a bed of its mother powder. A 1.6 mm thick strip of Au was sputtered onto one side of the pellet with a 1 mm gap in the center for the light source to excite the LLTO to eliminate possible effects on the impedance from illuminating the Au. Cu contacts were used to contact the sputtered Au to the 1260A Solartron impedance analyzer for EIS measurements. An open cell set-up was employed to allow THz irradiation to excite the sample without compromising average power.

The conductivity was then measured by an AC Impedance method over a frequency range of 32 MHz to 1 Hz with an applied 100 mV sinusoidal amplitude between 298 K – 333 K with and without the excitation source. A copper mesh faraday cage was custom-made with a 1.4 mm copper wire spacing to reduce the noise in EIS measurements due to electromagnetic interference from the environment.

For transient single frequency impedance measurements, an EIS scan from 1 MHz to 1 Hz was taken using a SP150 Biologic potentiostat to determine the frequency of the grain boundary intercept. The real, imaginary, and total impedance was then measured as a function of time (millisecond resolution) at the single frequency determined by the previous EIS step with and without the illuminated excitation source.

Section S3. Heating cell set up. A heating cell was custom made to heat the sample between 298 K – 333 K. The cell temperature was controlled using a TC-48-20 OEM temperature controller, 12 V power supply, and

corresponding TC-48-20 OEM software and thermocouple. The heating cell was placed inside a Faraday cage for all experiments to reduce noise from electromagnetic interference.

Section S4. Terahertz (THz) Setup.

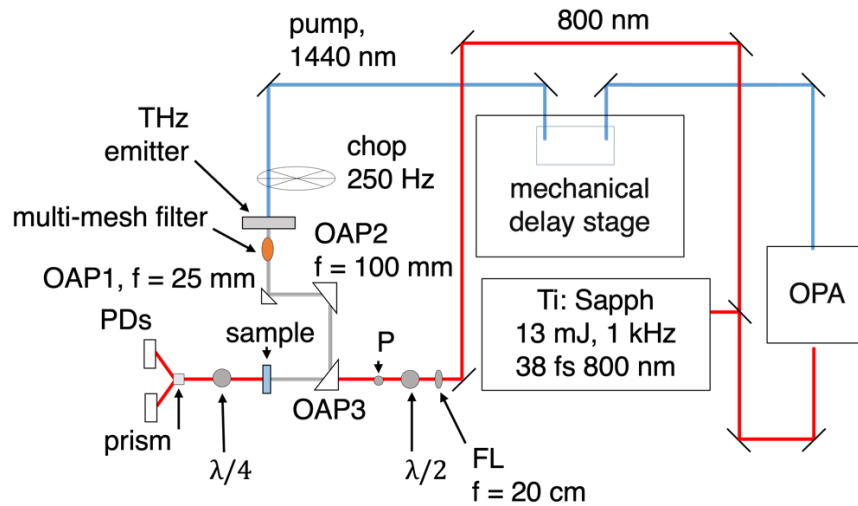


Diagram of the THz field set up. OPA: Optical Parameter Amplifier. OAP: Off-Axis Parabolic. FL: focal lens, P: polarizer, PDs: Photodiodes.

A 1 kHz, 38 fs, 13 mJ pulse centered at 800 nm produced via regenerative amplification in a Ti:Sapphire laser (Coherent Legend Elite Duo). The output beam is split by a 25:75 beam splitter, with the more intense ~ 10 mJ beam used to pump an optical parametric amplifier (OPA, TOPAS, Light Conversion Inc.), generating a 2.1 W, 1440 nm output signal beam. The signal beam goes through a mechanical delay stage and a chopper set at 250 Hz to reduce the average power to 1.1 W to not burn the DAST (4-*N,N*-dimethylamino-4'-*N'*-methyl-stilbazolium tosylate) crystal, which was purchased from Swiss Terahertz. The μ W output of the DAST crystal, which when focused through three OAPs into a ~ 250 μ m beam spot, gives a peak field intensity in the 100 kV/cm range. The chamber was purged under inert gas (N_2) to minimize water absorption and to increase the field strength of the THz source. The THz field was characterized using electro-optical detection in 30 μ m GaP.²

Section S5. Near-IR (NIR) to Mid-IR (MIR) Light Set-up. The NIR and MIR light sources were generated using a regenerative Ti:Sapphire laser amplifier operating at 1 kHz. The 800 nm output was sent through an optical parametric amplifier for the NIR light and a difference frequency generation unit for the MIR light.

Section S6. IR power to THz field strength. Terahertz pulse energies were measured using a calibrated pyroelectric THz joulemeter (Genotec EO SDX 1211). The subsequent THz field strength values were used to calculate an average power for comparison to the non-resonant heating.

Section S7. THz average power calculation.

$$\text{Pulse energy (J)} = \frac{\text{Voltage output (V)}}{614000 \text{ (V/J)}} \quad (1)$$

$$\text{Average power (W)} = \text{Pulse energy (J)} * \text{Repetition rate (Hz)} \quad (2)$$

Using a pyroelectric THz joulemeter, a measured voltage was used to calculate the pulse energy of the THz field using equation (1), where 614000 V/J is the conversion factor according to the manufacturer specifications. The average power of the laser was then calculated using equation (2) where J is the pulse energy and (symbol) is the repetition rate of the pulses after passing the chopper (500 Hz).

Table S1. IR power to THz field strength calibration yielding the average power calculation.

IR Pump Power (mW)	Field Strength (keV/cm)	Peak to Peak Voltage (V)	Average THz Power (mW)
1000	162.5	2.0	1.6
800	141.22	1.6	1.3
700	128.68	1.3	1.1
600	114.86	1.1	0.90
500	96.61	0.9	0.73
400	83.42	0.7	0.57
200	46.88	0.3	0.24

Section S8. General DFT setup. Li⁺ ion hop simulations in this study were conducted under the spin-polarized density functional theory (DFT) approximation using the Vienna Ab initio Simulation package (VASP)³ within the projector augmented-wave approach. Perdew–Burke–Ernzerhof (PBE)⁴ generalized-gradient approximation (GGA) functionals, electronic KPOINTS equal to 4x4x4, an electronic energy cutoff of 500 eV, and Gaussian smearing with sigma of 0.05 eV were employed for the calculations. The valence electrons for lanthanum, lithium, titanium, and oxygen atoms were generated in the 5s² 5p⁶ 5d¹ 6s², 1s² 2s¹, 3p⁶ 3d² 4s², and 2s² 2p⁴ configurations, respectively.

Section S9. Details for NEB calculations. The minimum energy pathway for Li⁺ ion hops in the lattice were calculated using the nudged elastic band (NEB) methodology following the formulations by Henkelman et al.⁵ to ensure the correct determination of the saddle point as implemented in VASP. Three middle images were considered for the NEB calculations. Structures at the end of the hops were relaxed to lower the forces and variations in energy below 10⁻⁴ eV/Å and 10⁻⁵ eV, respectively. Obtaining these end-point relaxed structures are critical in a successful NEB calculation to obtain meaningful migration barriers (MB). Because of the challenges in the convergence of DFT relaxation simulations, which is mainly caused by the multitude of relaxation sites available in the lattice of highly Li⁺ conductive compounds,⁶ different optimization algorithms were tested for the convergence of both local relaxed structures (corresponding to the beginning and end of the hops) and NEB calculations (reaction coordinates). The structure relaxation and NEB calculation were initially tested for convergence using conjugate-gradient energy-based optimization method (IBRION=2). If no convergence was

achieved using energy-based optimizers, force-based optimizers were then employed. Two force-based optimizers⁷ were identified to be effective in helping the convergence: (i) QM=Quick-Min (IOPT = 3, IBRION = 3, POTIM = 0), and (ii) FIRE = Fast Inertial Relaxation Engine (IOPT = 7, IBRION = 3, POTIM = 0). We reported the relaxed structure, the migration barrier (MB), the reaction coordinates using whichever method that converged. Afterwards, we utilized the reaction coordinates for the phonon modal analysis of the respective ion hop.

Section S10. Choosing the initial structure for computations. The same experimental structure identified from synchrotron X-ray diffraction of $\text{La}_{0.5}\text{Li}_{0.5}\text{TiO}_3$ in this study is used for the *ab initio* NEB and phononic calculations. For ease of calculations and better visualizations, the experimentally determined $R\bar{3}c$ structure ($a = b = 5.4711\text{\AA}$, $c = 13.4040\text{\AA}$, $\alpha = \beta = 90^\circ$, $\gamma = 120^\circ$) is transformed to its pseudo-cubic (perovskite-looking) counterpart⁸ ($a = b = c = 7.7378\text{\AA}$, $\alpha = \beta = \gamma = 90^\circ$) through the rotation/transformation of the lattice based on the formula below:

$$R = R_z(\alpha)R_x(\gamma)R_y(\beta) = \begin{bmatrix} \cos(\alpha) & -\sin(\alpha) & 0 \\ \sin(\alpha) & \cos(\alpha) & 0 \\ 0 & 0 & 1 \end{bmatrix} \begin{bmatrix} 1 & 0 & 0 \\ 0 & \cos(\gamma) & -\sin(\gamma) \\ 0 & \sin(\gamma) & \cos(\gamma) \end{bmatrix} \begin{bmatrix} \cos(\beta) & 0 & \sin(\beta) \\ 0 & 1 & 0 \\ -\sin(\beta) & 0 & \cos(\beta) \end{bmatrix}$$

where, $\alpha = 0^\circ$, $\gamma = -45^\circ$, and $\beta = -35^\circ$ correspond to yaw, roll, and pitch angles, respectively. We considered 40 atoms in this pseudo-cubic unit cell, and we used it for the rest of our simulations. After the transformation, only internal atomic coordinates were relaxed during the calculations.

Section S11. Maximizing the sampling of Li^+ hop in the LLTO lattice through different choices of lattice disorder, Li^+ hopping mechanisms, and hopping pathways. The experimentally determined coordinates for La and Li contain partial occupancies, and need to be substituted with atoms in order to perform atomistic simulations. It is important to maintain the exact experimental stoichiometry ($\text{La}_{0.5}\text{Li}_{0.5}\text{TiO}_3$) during this process. Depending on which La and Li partial occupancy sites are selected for atom placement in the simulation, locally different structures of LLTO can be formed. Experimental⁹ and computational¹⁰⁻¹² studies have shown that the various structures of LLTO can be classified into three categories based on the degree of La|Li disorder in the lattice (Li|La orderings): (i) fully ordered structure, (ii) partially ordered structure, and (iii) fully disordered structure. However, due to the limited size of the supercell used in our simulations (40 atoms), it is difficult to distinguish between the partially ordered and fully disordered structures. Therefore, to maximize our sampling of Li^+ ion hops in the LLTO lattice within the constraints of our supercell size, we included three different La|Li orderings in our analysis of Li^+ ion hops, as illustrated in **Fig. S15**. These chosen structures included one structure with ordered Li|La layers, as well as two structures with disordered Li|La layers.

Since our calculations do not involve any hopping for La atoms, the position of La atoms is the primary factor that distinguishes these three structures with different La|Li orderings. Therefore, these structures can be regarded as parent structures, under which we have defined several substructures by shuffling Li^+ ions among unoccupied sites in the LLTO lattice. Although our simulation cell sizes may not be large enough to fully capture the exact differences between these parent structures with different La|Li orderings, we believe that incorporating these different ordered and disordered parent structures, along with their substructures and the different Li^+ hopping mechanisms included in these substructures, has increased our sampling of different local chemical environments in the LLTO lattice in our calculations. The schematics of the parent structures with different Li|La ordering

layers, the number of Li⁺ hops calculated for different substructures under these parent structures obtained by shuffling Li⁺ ions in the lattice or along different hopping pathways, and the different considered hopping mechanisms are illustrated in **Fig. S15**.

In addition to the different degrees of disorder in the LLTO lattice, we also considered two different hopping mechanisms: (i) single and (ii) concerted ion hops. For the single ion hop mechanism, the hop occurs through a vacancy. However, there are no vacancy sites in the stoichiometry considered in this study (i.e., the nominal number of vacancies in the stoichiometric La_{2/3-x}Li_x□_{1/3-2x/3}TiO₃ for x=1/2 is zero). To allow the occurrence of the vacancy-mediated mechanism, a La cage must be doubly occupied by two Li⁺ ions. This results in an unoccupied La cage that was previously occupied, which is now available for other Li⁺ ions to hop into. Thus, the choice of the doubly occupied La cage and the resulting hopping pathway will be the determining factor for performing our NEB calculations. We combined different (i) orderings of Li|La, (ii) choices of which La cage to doubly occupy, and (iii) hopping mechanisms to choose 22 different Li⁺ hopping events to maximize our sampling efficiency of the LLTO lattice. The distribution of the different hopping mechanisms (single and concerted) across the chosen structures with different degrees of disorder is illustrated in **Fig. S15**.

Section S12. DFPT setup for modal calculations. To obtain the vibrational modes (phonons) for each of the structures considered in this study, we first calculated the Hessian matrix using density-functional-perturbation theory (DFPT) with the VASP software and the Phonopy package¹³ to capture the matrix. Next, we calculated the phonon frequencies and eigenvectors using a custom lattice-dynamics Python code.¹⁴ It was important to obtain these values for the exact supercell containing 40 atoms, since the NEB calculations were also performed on cells of this size.

Section S13. Phonon modal analysis of ion hop. To identify the contribution of different phonons to the Li⁺ hop in the lattice, we used the methodology recently proposed based on combining the lattice dynamics and NEB calculations.¹⁵ Following this method, after the minimum energy pathway for the Li⁺ hop is identified using the NEB calculation, we project the displacement field obtained from the transition state (saddle point) on the eigenvectors of vibration belonging to the structure at the beginning of the hop. The magnitude of projection shows the degree to which each normal mode is contributing to that displacement field, which can be quantified using the following expression,^{16,17}

$$Q_n = \sum_{i=1}^N \sqrt{m_i} \mathbf{e}_{i,n}^* \cdot \mathbf{u}_i \quad (3)$$

where \mathbf{u}_i is the displacement of atom i from its equilibrium position in the configuration at the hopping origin; $\mathbf{e}_{i,n}$ is the eigenvector for mode n , assigning the direction and displacement magnitude of atom i obtained from the lattice dynamics calculation^{16,18,19} for the structure at the hopping origin; * denotes the complex conjugate operator; and m_i is the mass of atom i . Q_n is the modal displacement coordinate, the square of which is proportional to the mode potential energy E_n according to the following equation,¹⁷

$$E_n = \frac{1}{2} \omega_n^2 Q_n^2 \quad (4)$$

The total energy of the system E is equal to the summation over all modal energy values ($E = \sum_n E_n$); Here, E_n is the contribution by mode n to the potential energy of the displaced lattice during the ion migration, which can be interpreted as the contribution by mode n to the ion hop along its migration pathway. In addition, ω_n is the frequency of vibration of mode n . E_n can be divided by E to calculate the normalized contribution of that phonon to the Li^+ hop in that specific ion hop event. Moreover, by subsequently normalizing E_n through division by the total number of ion hopping events considered in the study, the resultant normalized E_n can be regarded as the normalized contribution of mode n to the Li^+ hopping events in the LLTO compound under investigation. The code used to identify the modal contributions of Li^+ hop in the LLTO lattice, following the outlined methodology, was written in Python and is available as a GitHub repository.¹⁴

Section S14. Algorithm for identifying the rocking modes. In this study, we identified the octahedral modes of vibration by quantifying the degree of circulation the eigenvectors of vibration impose on the octahedron units (TiO_6) in the lattice. To this end, the eigenvectors of vibration for the 6 oxygen atoms belonging to the TiO_6 octahedron unit were utilized to quantify the circulation of the unit according to the definition of circulation (Γ), e.g., $\Gamma_n^i = \oint \vec{v} \cdot \vec{dl}$, where Γ_n^i is the circulation belonging to the octahedron unit i (in our case we have 8 octahedron units in our simulation cells, thus $i = \{1, 2, 3, \dots, 8\}$) coming from mode of vibration n . In addition, \vec{dl} is the path vector along which the circulation is being evaluated, and \vec{v} is the eigenvector of vibration belonging to the specific atoms along the \vec{dl} direction. In practicality, to simplify the evaluation of the circulation formula above, we considered the perfect representation of a perovskite structure (e.g., with untitled octahedron units) and evaluated Γ_n^i along the circulation pathways normal to x , y , and z directions, which results in $\Gamma_n^{i,\alpha} \{\alpha = x, y, z\}$. By averaging the obtained values of $\Gamma_n^{i,\alpha}$ over α , a representative circulation value is found for octahedron unit number i (Γ_n^i). By averaging again over all the octahedron units in the simulation cell, i , a representative value of circulation is obtained for all the octahedron units in the simulation cell (Γ_n). If this value is larger than a specified criterion, the mode of vibration number n is identified as an octahedral mode of vibration. Example MATLAB code block below demonstrates this calculation:

```
% modenum = 3*Natoms % number of modes of vibration in the system
for n=1:modenum
    vortTi = zeros(8, 3);
    % TiO6 unit 1 (atomids listed below)
    ix1 = 23;
    ix2 = 26;
    iy1 = 21;
    iy2 = 27;
    iz1 = 34;
    iz2 = 36;
    vortTi(1,1) = (ev((iy2-1)*3+3, n) - ev((iy1-1)*3+3, n)) - (ev((iz2-1)*3+2, n) - ev((iz1-1)*3+2, n));
    vortTi(1,2) = (ev((iz2-1)*3+1, n) - ev((iz1-1)*3+1, n)) - (ev((ix2-1)*3+3, n) - ev((ix1-3)*3+3, n));
    vortTi(1,3) = (ev((ix2-1)*3+2, n) - ev((ix1-1)*3+2, n)) - (ev((iy2-1)*3+1, n) - ev((iy1-1)*3+1, n));
    .
    .
    .
    for ii=1:8
        vortTi_mag(ii) = (vortTi(ii,1)^2 + vortTi(ii,2)^2 + vortTi(ii,3)^2)^.5;
    end
    vortTi_ave(n) = mean(vortTi_mag);
    vortTi_mag_allmodes(n, :) = vortTi_mag;
end
tagOctRot(1:modenum, i) = 0;
for n=1:modenum
    vorticity_criteria = 0.25;
    if vortTi_ave(n)^2 > vorticity_criteria
        tagOctRot(n) = 1;
    end
end
end
```

Section S15. Calculating the imparted energy on different atomic species by different modes of vibration.

To calculate the energy that each mode of vibration imposes on the hopping Li^+ , we leverage the following identity equation existing from lattice dynamics theory,¹⁷ $\sum_n \vec{v}_n^i \cdot \vec{v}_n^i = 1$, where \vec{v}_n^i is the eigenvector of vibration belonging to mode n , imposing vibrations on atom i . The vibrations of atoms in the crystal are governed by the eigenvectors of vibration, and the imparted vibrations on an atom will add up to give an energy equal to $k_B T$ to that atom. In this view, the $\vec{v}_n^i \cdot \vec{v}_n^i$ term in the summation above can be considered to be proportional to $k_B T$. This methodology can be extended to the eigenvectors of vibration on the hopping Li^+ , where they can be projected along the hopping direction of the Li^+ to give the energy imparted on Li^+ along the hopping pathway, e.g., $E_{\text{Li}^+}^{\text{hopping direction}} = \vec{v}_n^{\text{Li}^+} \cdot \vec{u}_{\text{hopping direction}}$. Similarly, the $\vec{v}_n^{\text{Li}^+} \cdot \vec{u}_{\text{hopping direction}}$ term can be considered to be proportional to $k_B T$.

Section S16. Quantifying the change in O-4 bottleneck area due to phonon modes in the structure.

To evaluate the impact of each phonon on the O-4 bottleneck area during ion hopping, we applied a displacement to the lattice along the eigenvectors associated with that phonon. This displacement can be considered as an induced excitation of the lattice. The extent of this excitation can be calculated for each vibrational mode using the following equations.

The potential energy for an oscillator can be written as arising from the sum of harmonic and anharmonic contributions,¹⁷

$$\langle H_{\text{pot}} \rangle = \langle H_{\text{harmonic}} \rangle + \langle H_{\text{anharmonic}} \rangle \quad (5)$$

where $\langle \dots \rangle$ represents the ensemble average.²⁰ The harmonic portion has been shown to dominate the potential energy.²¹ Thus, we will also leverage the harmonic potential energy to evaluate the mode amplitude that is needed to calculate the degree of displacement field in the structure. Based on the equipartition theorem, the average harmonic energy of a classical oscillator is equal to,²²

$$\langle H_{\text{harmonic}} \rangle = \frac{1}{2} k_B T \quad (6)$$

Where k_B is the Boltzmann constant, and T is the temperature of the system. The potential energy of a harmonic oscillator can also be calculated from the normal mode amplitude analysis via Eq. 4,¹⁷

$$\langle H_{\text{harmonic}} \rangle = \frac{1}{2} Q_n^2 \omega_n^2 \quad (7)$$

where Q_n is the modal displacement coordinate (Eq. 3), and ω_n is the frequency of the eigen mode. It should be noted that calculating the harmonic energy of an eigen mode using the knowledge of force constant matrix and the respective atomic displacements for an eigen mode is equal to the approach based on the normal mode amplitude analysis (Eq. 7). The modal displacement coordinate can be explicitly obtained from Eq. 3, which is rewritten here,¹⁷

$$Q_n = \sum_{i=1}^N \sqrt{m_i} \mathbf{e}_{i,n}^* \cdot \mathbf{u}_i \quad (3)$$

where \mathbf{u}_i is the displacement of atom i from its equilibrium position in the configuration at the hopping origin; $\mathbf{e}_{i,n}$ is the eigenvector for mode n , assigning the direction and displacement magnitude of atom i obtained from the lattice dynamics calculation^{16,18,19} for the structure at the hopping origin; $*$ denotes the complex conjugate operator; and m_i is the mass of atom i . By combining Eq. 6 and Eq. 7 we then have,

$$Q_n^2 \omega^2 = k_B T \quad (8)$$

To determine the distribution of the harmonic energy for eigen mode amongst the atoms in the system, one can envision a state of the system whereby all of the atoms in the system are displaced from equilibrium in the direction of their respective eigen vectors from mode \mathbf{n} (i.e., $\mathbf{e}_{i,n}$). In this view, the attributed displacement to an atom would be equal to,

$$\mathbf{u}_i = \alpha_n \mathbf{e}_{i,n} \quad (9)$$

Where α_n is a scaling factor that associates a certain degree of displacement with the mode's amplitude at a given temperature. The exact value of the scaling factor can then be calculated from the combination of Eq. 3, Eq. 8 and Eq. 9. Replacing for the atomic displacement in Eq. 3 with the definition in Eq. 9, we would have,

$$Q_n = \sum_{i=1}^N \sqrt{m_i} \mathbf{e}_{i,n}^* \cdot \alpha_n \mathbf{e}_{i,n} = \alpha_n \sum_{i=1}^N \sqrt{m_i} \mathbf{e}_{i,n}^* \cdot \mathbf{e}_{i,n} \quad (10)$$

which by the substitution of $Q_{i,n} = \sqrt{m_i} \mathbf{e}_{i,n}^* \cdot \mathbf{e}_{i,n}$, yields a simpler form,

$$Q_n = \alpha_n \left(\sum_{i=1}^N Q_{i,n} \right) \quad (11)$$

Using Eq. 8 we then have $Q_n \omega_n = \sqrt{k_B T}$ and by incorporating Eq. 11, we can calculate the scaling factor as,

$$\alpha_n = \frac{\sqrt{k_B T}}{\left(\sum_{i=1}^N Q_{i,n} \right) \cdot \omega_n} \quad (12)$$

By using the obtained α_n in Eq. 9, the displacement field is obtained. The O-4 bottleneck area will then be calculated for both the equilibrium (no displacement) lattice and the lattice for which the atomic positions have been displaced according to Eq. 9 to assess the capability of each phonon in increasing the O-4 bottleneck area against the ion hop. It should be noted that the four oxygen atoms forming the bottleneck area are not necessarily on the same plane in space, making it impossible to calculate the planar area connecting them. Therefore, four smaller triangular areas inside the bottleneck area are defined (as shown in **Fig. S17**), and their areas are calculated and averaged to approximate the bottleneck area in this situation, as demonstrated in **Fig. S17**. The percent change

between the O-4 bottleneck area in the equilibrium lattice and the one in the displaced lattice is then calculated and reported as the change in the ability of that specific phonon in altering the bottleneck area against the hop of Li⁺ ion.

Section S17. Quantum correcting the calculated modal contributions to the ion hop. To include the quantum effects in our reported modal contributions to the Li⁺ hop in LLTO, we multiply our obtained modal contribution by mode n (E_n , obtained from Eq. 4) with frequency ω by a correction coefficient that is based on the Bose-Einstein distribution function at temperature T ($f_Q(\omega, T)$) based on the following formula to obtain the quantum corrected contribution of that mode n to the hop in the lattice (E_n^{qc}),¹⁶

$$E_n^{qc}(\omega) = f_Q(\omega, T)E_n(\omega) \quad (13)$$

The function f_Q represents the ratio of quantum to classical specific heat for mode n . It restricts the contributions of the high frequency modes at low temperatures and modulates the modal contributions obtained from the NEB-based ion hop simulations. The quantum expression of volumetric specific heat, based on Bose-Einstein statistics, is given by

$$C_q(\omega, T) = \frac{k_B x^2}{V} \frac{e^x}{(e^x - 1)^2}; x = \frac{\hbar\omega}{k_B T}, \quad (14)$$

and the classical volumetric specific heat is given by $C_c = \frac{k_B}{V}$, where V is the volume of the supercell under study. Thus, the quantum heat capacity correction factor which is the ratio of C_q and C_c is

$$f_Q(\omega, T) = \frac{C_q(\omega, T)}{C_c} = \frac{x^2 e^x}{(e^x - 1)^2} \quad (15)$$

Section S18. Enhancing ion hopping rate by targeted excitation of phonons in MD simulations. To assess if any increase in the hopping rate of Li⁺ in LLTO lattice can happen by exciting the identified contributing phonons to the ion hop, we chose three hops from the 22 investigated hops in this study. We then excited the highly contributing phonons in their respective structures. We performed the following three tests: (i) exciting the top contributing (non-rocking) mode overall, (ii) exciting the top contributing rocking mode, and (iii) exciting a random mode.

To perform the molecular dynamics simulations, we utilized classical molecular dynamics simulations based on the Morse and Buckingham form potentials as proposed by Cormack and coworkers^{23,24} and successfully utilized by Chen and Du²⁵ to investigate the diffusion of Li⁺ diffusion in the LLTO lattice. The simulations were performed using the same DFT simulation cells using the large-scale atomic/molecular massively parallel simulator (LAMMPS)²⁶ package. The modes that were excited were the same modes that were detected from the DFT calculations. The goal of these experiments was to only assess if any extra energy (excitation) given to this highly contributing modes will result in any enhancement in the hopping rate of ion in the lattice.

First, the structure was relaxed under the under the Nosé-Hoover canonical ensemble for 100 ps at $T = 400$ K; then, the structure was simulated until a Li⁺ hops in the structure. Once the hop gets detected through continuous

examination of equilibrium MD positions during the MD simulation,¹⁵ the simulation gets interrupted and restarted with a new initial condition for atomic velocities, which results in exploring a new region of the phase space. This process gets repeated until a total of 50 ns has been simulated. Then the total number of detected ion hops will be compared based on the group of phonons that were excited during the simulations. The time step was chosen to be 1 fs.

Because ion diffusivity increases with temperature, we ensured that the bulk lattice temperature remained constant at a low temperature ($T = 400$ K), so that any change in the diffusivity could be attributed only to the excitation of the targeted modes and not to the bulk temperature. To do so, we kept the total kinetic energy of the system constant via a velocity-rescaling scheme, in which, the addition of energy to the intended modes was complimented by a uniform reduction in the kinetic energy of all other modes in the system. To change the temperature of mode n to a desired temperature T_d , we modified the atomic velocities in the system according to the following formula:

$$\mathbf{v}_i = \mathbf{v}_i + \frac{1}{\sqrt{m_i}} [\sqrt{2k_B T_d} - \dot{Q}_n(t)] \mathbf{e}_{i,n} \quad (16)$$

where \mathbf{v}_i is the velocity of atom i , and \dot{Q}_n is the modal velocity coordinate of mode n defined by,¹⁷

$$\dot{Q}_n = \sum_{i=1}^N \sqrt{m_i} \mathbf{e}_{i,n}^* \cdot \mathbf{v}_i \quad (17)$$

In this study, the above-mentioned rescaling procedure was applied every five-times steps (every 5 fs). Although a velocity-perturbation scheme has been used in this study, other methods for modal excitation, such as atomic position perturbation²⁷ or simultaneous perturbation of atomic positions and velocities,²⁸ have also been employed in previous studies, particularly those with the goal of investigating the phonon-phonon interactions in MD simulations. However, the chosen method for modal excitation should not change the reported observations in this study because modal excitation (increasing the energy of a mode) can be achieved either by increasing the potential (position perturbation) or the kinetic (velocity perturbation) energy of the mode; the choice of which should not matter.

The results for the excitations are shown in Table S4. By targeted excitation of the detected contributing phonons in the LLTO structure (including the contributing rocking modes), the hopping rate of the Li^+ increases to the same order magnitude of increasing the hopping rate by increasing the temperature, but this time, by keeping the lattice at the base ($T = 400$ K) temperature.

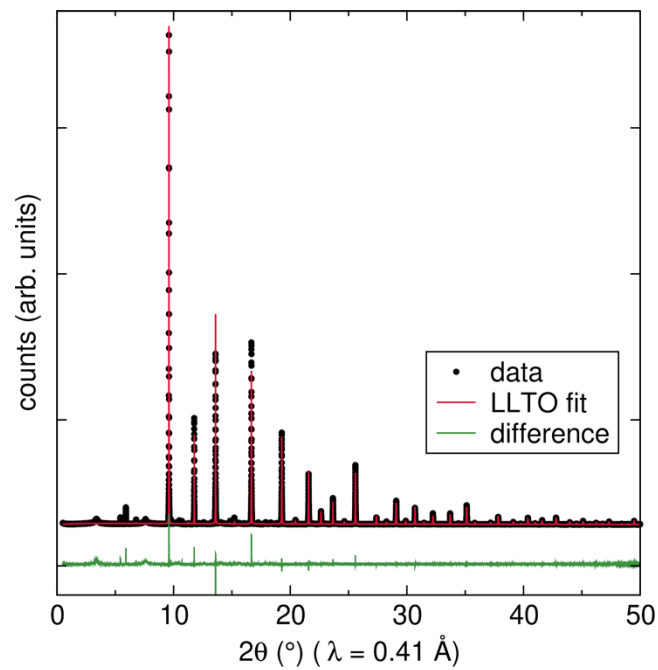


Figure S1. Synchrotron X-ray diffraction of LLTO. Small peaks found below 10 \AA^{-1} correspond to impurities.

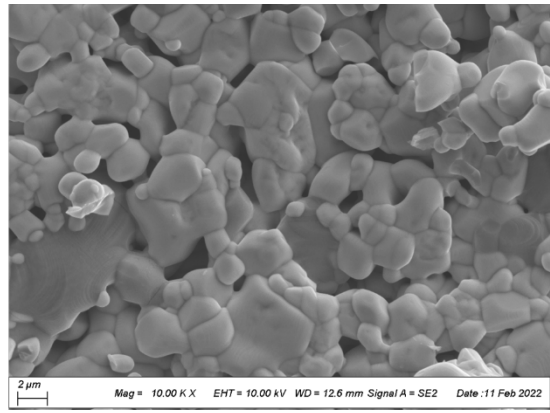
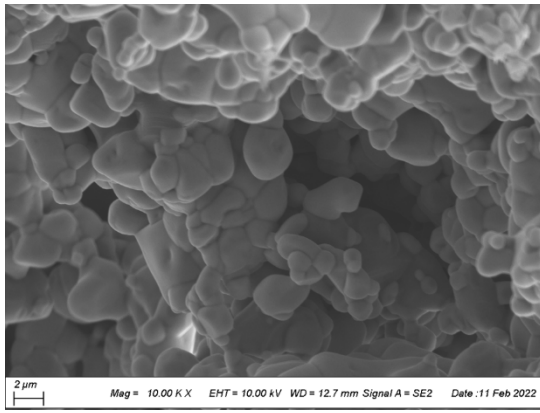


Figure S2. SEM image of LLTO (left) looking down the cross-section, and (right) on the surface of the annealed LLTO pellet. Grains are 1-10 μm in size.



Figure S3. Image of LLTO pellet with Au sputtered contacts.

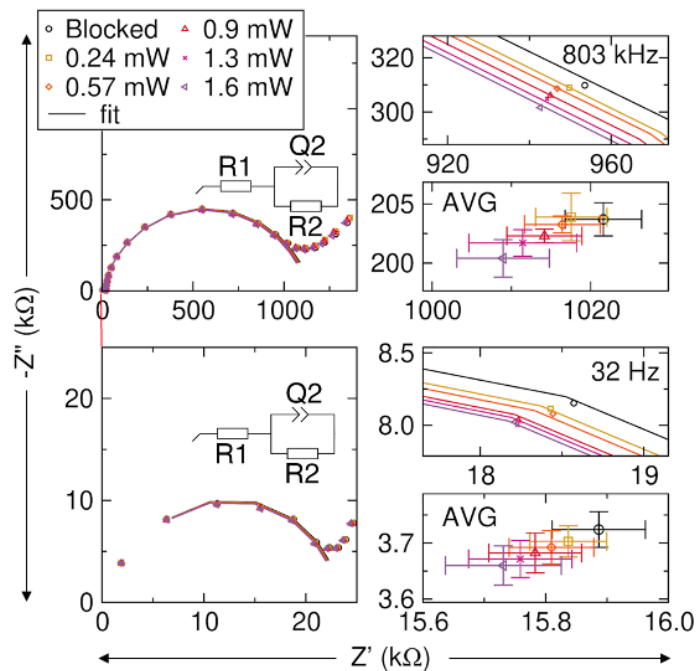


Figure S4. EIS showing the shift in bulk and grain boundary impedance upon illumination by broadband THz, with each semi-circle fitted to an $R1+R2/Q2$ equivalent circuit. The 803 kHz and 32 Hz panels show the EIS fits zoomed in. The AVG (average) panels show the impedance at the same single frequencies and error bars associated with the measurement.

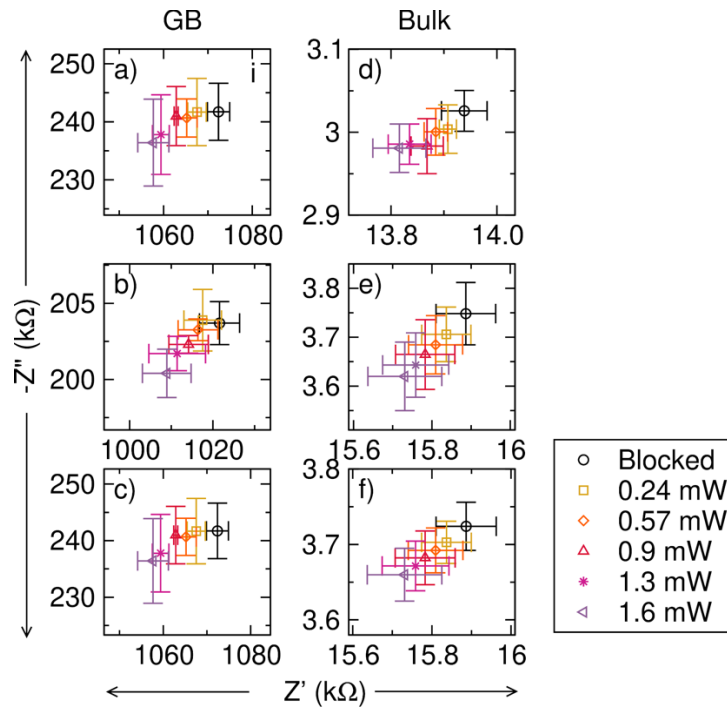


Figure S5. (a-c) Single frequency impedance measurements at 32 Hz for grain boundary features and (d-f) at 803 kHz for the bulk features averaged over 3 samples and 4 trials. The frequency chosen represents the frequency at which the greatest difference is observed between the Nyquist plots at points close to the Z' intercept. The frequency is different from the intercepts shown **fig. 3a** and **3b** because of the change in cell set up (and subsequent change in cell pressure). Although the absolute impedance varies slightly, the relative changes are consistent between sample to sample.

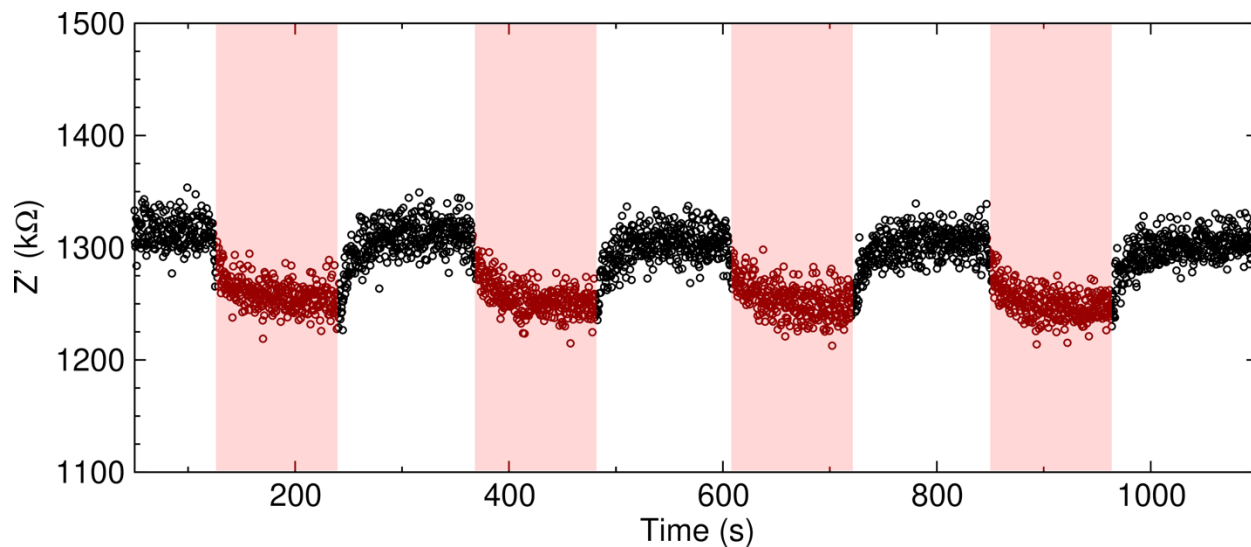


Figure S6. Growth and decay of the total impedance of LLTO upon illumination and subsequent removal of the 800 nm light source at 25 mW. The dark total impedance decreases to the illuminated impedance measurement in approximately 60 seconds, highlighted in red boxes. The total impedance returns to the dark state in approximately 90 seconds upon removal of the 800 nm source.

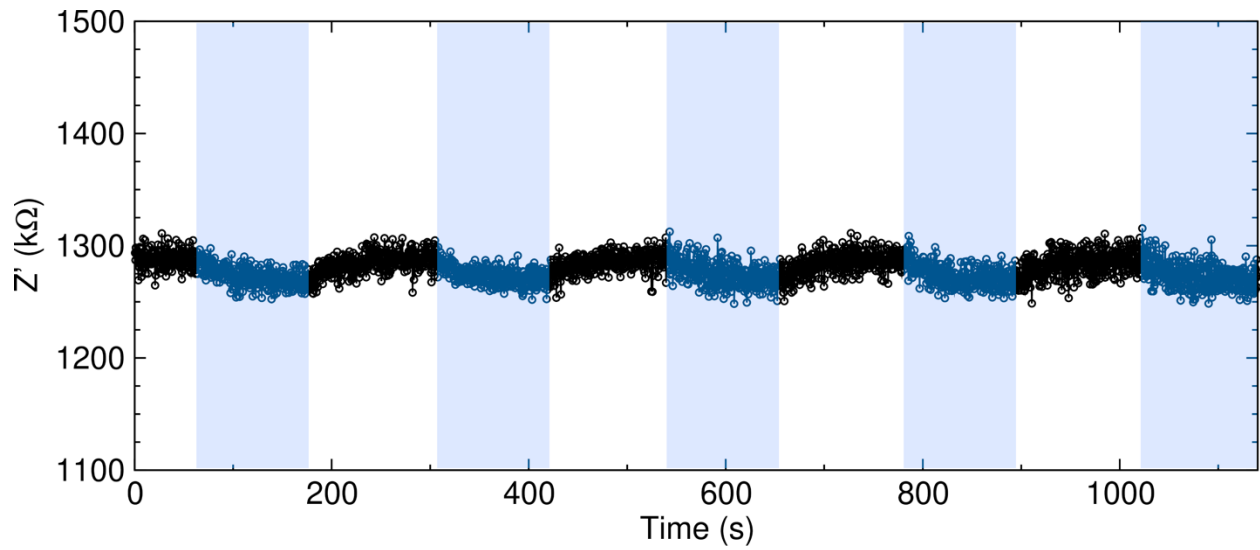


Figure S7. Growth and decay of the total impedance of LLTO upon illumination and subsequent removal of the THz field source at 1.6 mW. The total impedance relaxes from the illuminated state to dark impedance measurement in approximately 100 seconds. The total impedance returns to the excited state from dark state upon illumination in approximately 100 seconds.

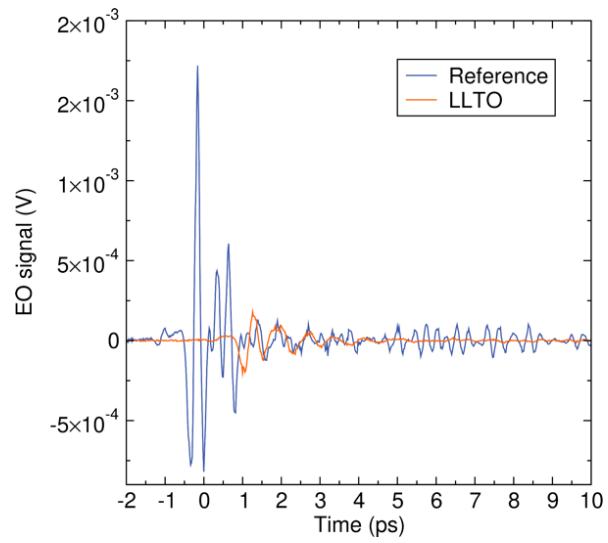


Figure S8. THz time domain trace with and without LLTO. The drop in EO signal with the LLTO sample indicates the absorption of the THz field by the sample.

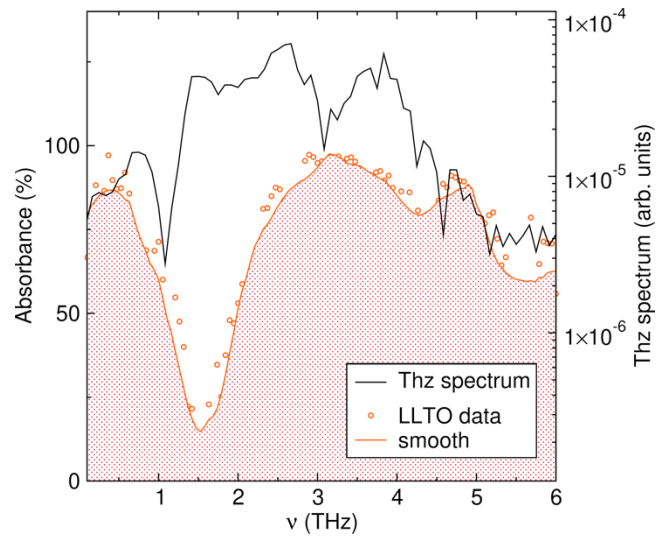


Figure S9. THz spectrum (grey) compared to the measured absorption (red). The decrease in THz amplitude around 1.1 THz and ~ 3 THz correspond to multiple phonon absorption bands in the DAST.²⁹

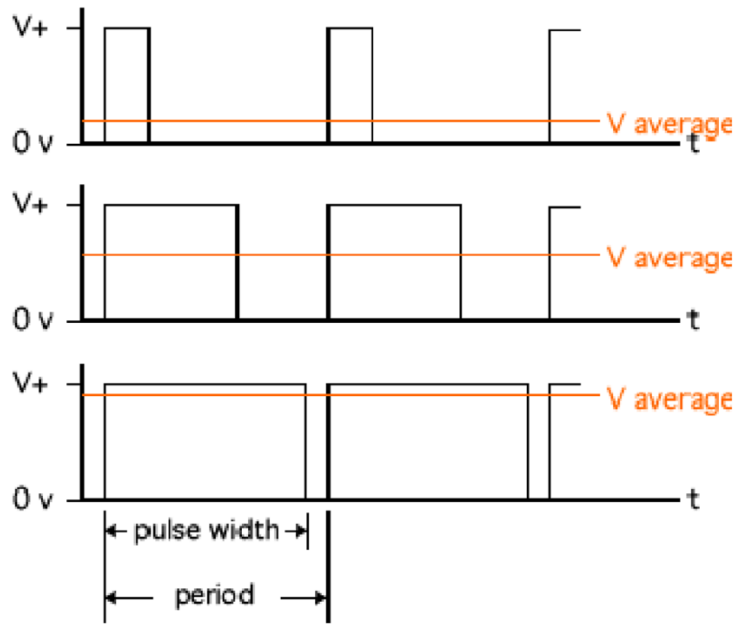


Figure S10. To generate the correct temperature, the TC-48-20 OEM regulates the output power to the TE device using a pulse width modulation. The power is turned “on” and “off” at 337 Hz to create a square wave “pulse”. The “on” time, or pulse width, is varied to create an average output. The mechanics of generating the average power is like that of the average power measured by a power meter, thus we create a calibration curve to determine the approximate change in temperature based on output power for the various irradiation sources used. Adapted from TC-48-20 OEM manual.

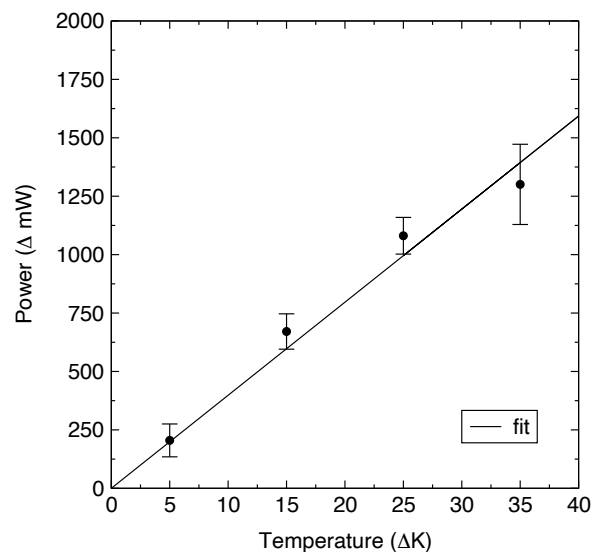


Figure S11. A Fluke 87-V Digital Multimeter was used to measure the current output of the temperature controller at varying temperatures between 298 K – 333 K. We quantitatively compared the effect of light with that caused by heat, or non-resonant thermalization, by designing a custom heating cell set-up with a controlled, ceramic heating plate. The change in impedance due to heating was then correlated with the power supply’s power input. The accurate correlation between heating from the electrical power and optical power suggested that any change in impedance that is greater than those caused by laser thermalization can be attributed to resonant excitation interactions. The corresponding power was calculated using the measured current output and the output voltage (12 V). A change in one kelvin is approximately equal to an input power of 39.8 mW.

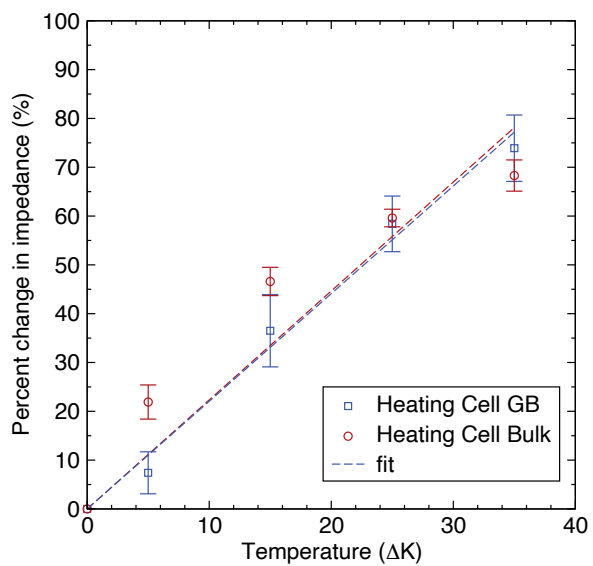


Figure S12. The percent change in impedance as a function of temperature. A 2.20% change in R_{GB} correlates to a 1 K change ($R^2 = 0.9955$) and 2.23% for R_{BULK} ($R^2 = 0.9634$).

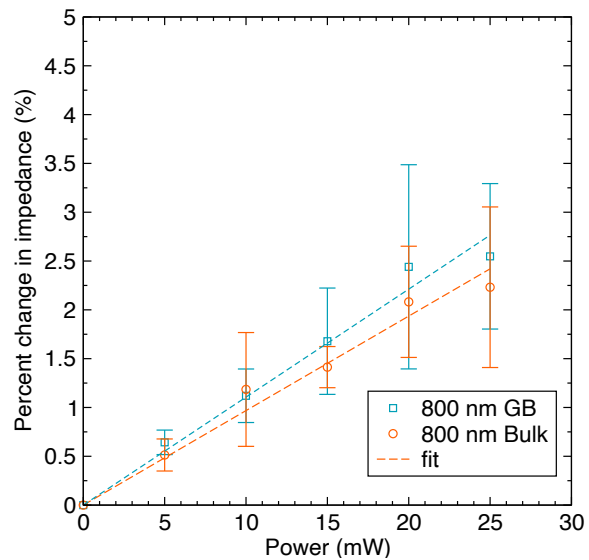


Figure S13. The percent change in impedance as a function of power using a 1kHz pulsed 800 nm laser with a 250 μm beam diameter. 1 mW of power causes a 0.11% change in grain boundary impedance ($R^2 = 0.9936$) and 0.10% in bulk impedance ($R^2 = 0.9918$).

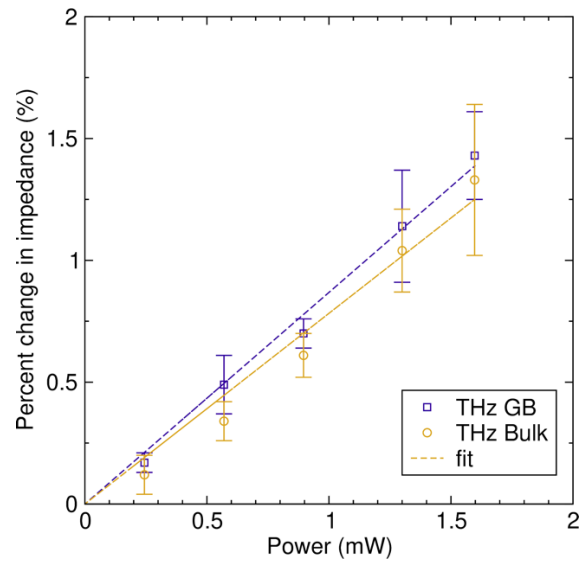


Figure S14. The percent change in impedance as a function of power using a broadband 0.5 – 6 THz field with a ~ 250 μm beam spot. 1 mW of power causes a 0.87% change in grain boundary impedance ($R^2 = 0.9976$) and 0.78% change in bulk impedance ($R^2 = 0.9905$).

Table S2. Overview of the % change in R_{bulk} with various normalization values. Bulk heating values are approximated using the conversion factor 39.8 mW to 1 K from fig. S6. For the power density normalization, a 250 μm beam diameter was assumed for 800 nm and $\sim 250 \mu\text{m}$ beam spot for THz. The standard deviation for each value is shown in italics.

Excitation	% Change in R_{bulk}/ mW	% Change in R_{bulk}/ Power Density (mW/cm^2)	% Change in R_{bulk}/ ΔK
Non-resonant, pulsed (800 nm)	0.12 ± 0.03	$5.0 \times 10^{-5} \pm 1.7 \times 10^{-5}$	$3.98 \pm 1.2^*$
THz pulsed (0.5 – 5 THz)	0.68 ± 0.14	$4.8 \times 10^{-4} \pm 1.3 \times 10^{-4}$	$31.0 \pm 7.2^*$
Bulk Heating (25 – 60 °C)	$0.07 \pm 0.03^*$	--	2.96 ± 1.1
Optical phonons (12.9 μm)	0	0	0

Table S3: Overview of the % change in R_{GB} with various normalization values. Bulk heating values are approximated using the conversion factor 39.8 mW to 1 K from Fig. S6. For the power density normalization, a 250 μm beam diameter was assumed for 800 nm and 300 μm for THz. The standard deviation for each value is shown in italics.

Excitation	% Change in R_{gb}/mW	% Change in $R_{gb}/$ Power Density (mW/cm^2)	% Change in $R_{gb}/\Delta K$
Non-resonant, pulsed (800 nm)	0.10 ± 0.03	$5.7 \times 10^{-5} \pm 1.6 \times 10^{-5}$	$4.38 \pm 1.2^*$
THz pulsed (0.5 – 5 THz)	0.82 ± 0.09	$5.8 \times 10^{-4} \pm 1 \times 10^{-4}$	$34.6 \pm 5.6^*$
Bulk Heating (25 – 60 °C)	$0.05 \pm 0.01^*$	--	2.09 ± 0.4
Optical phonons (12.9 μm)	0	0	0

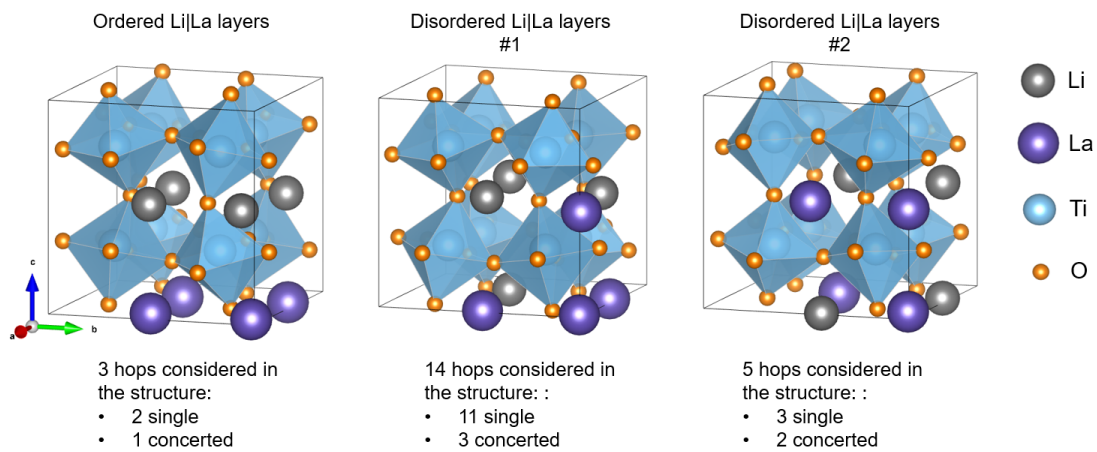


Figure S15. Schematics of three different Li|La orderings with respect to the c -axis in the $\text{La}_{0.5}\text{Li}_{0.5}\text{TiO}_3$ lattice included in our calculations. The chosen number of Li^+ ion hops with different hopping mechanisms are also included in the bottom of the schematics.

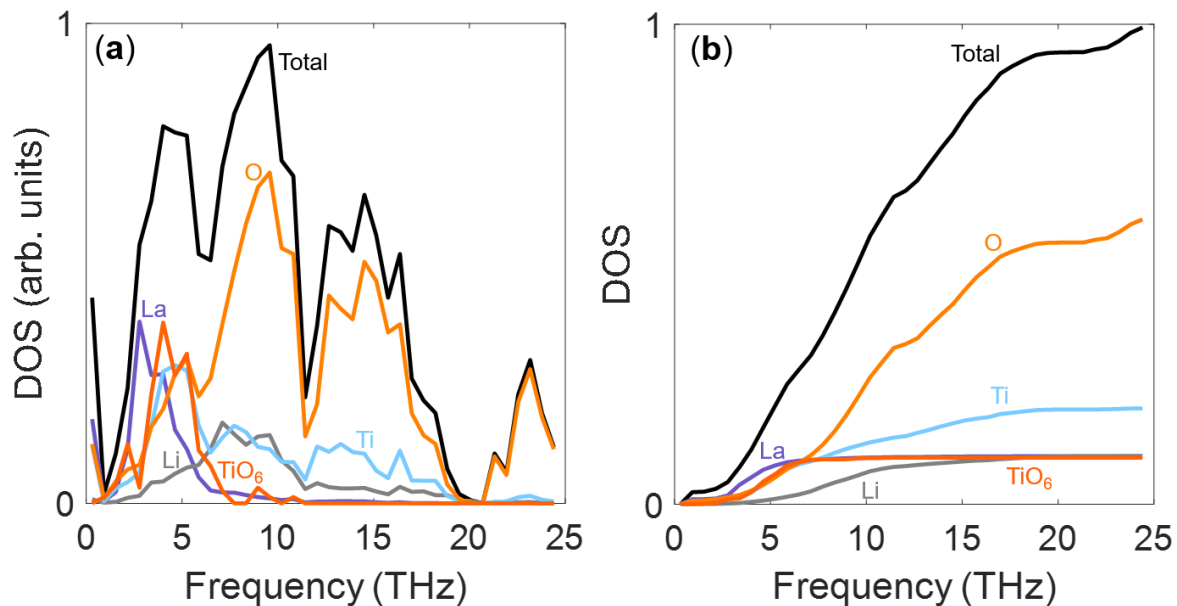


Figure S16. Total and partial phonon density of states in (a) non-accumulation and (b) accumulation format for different atomic species and rocking modes (TiO₆ units). Accumulation format helps revealing useful information. For instance, it shows that 10 % of the total modes are of TiO₆ rocking nature, and in the <6THz region, 36% of the modes are of TiO₆ rocking nature.

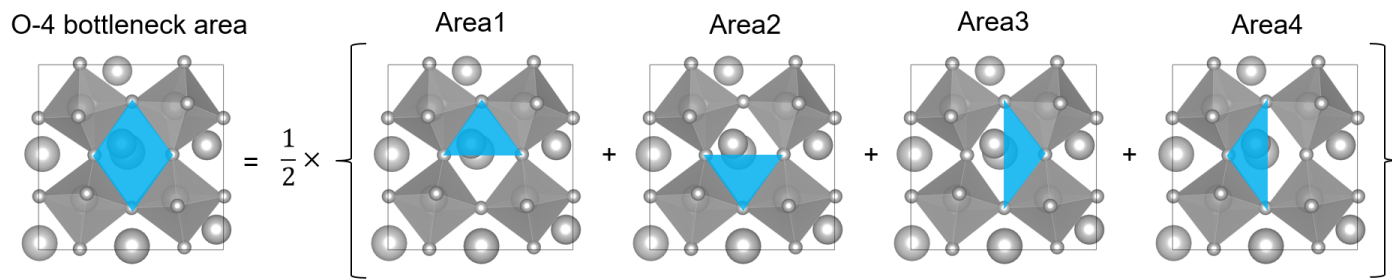


Figure S17. The O-4 bottleneck area in space is approximated by averaging over four smaller triangular areas (shown by transparent blue).

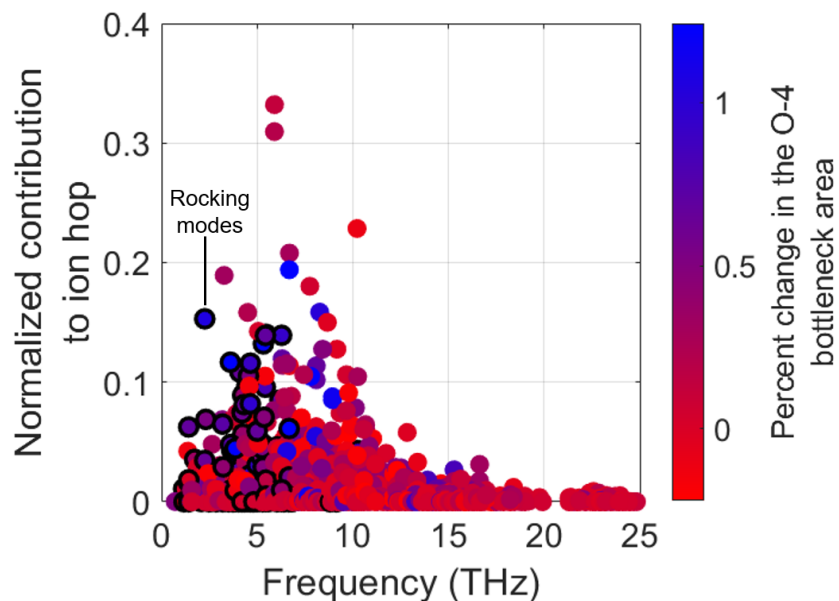


Figure S18. Scatter plot displaying the normalized individual contributions of phonons to the Li^+ ion hop in the LLTO lattice. The color of each data point represents the extent to which the corresponding phonon can modify the O-4 bottleneck area against the hopping of Li^+ ions in the lattice, with the color bar indicating the percentage of change in the bottleneck area, calculated using the methodology explained in Section S16. Positive percent changes refer to widening of the bottleneck while negative percent changes refer to shrinkage of the bottleneck. Rocking modes, indicated by black rings surrounding their data points, exhibit a comparatively higher ability to modify the O-4 bottleneck area in comparison to non-rocking modes.

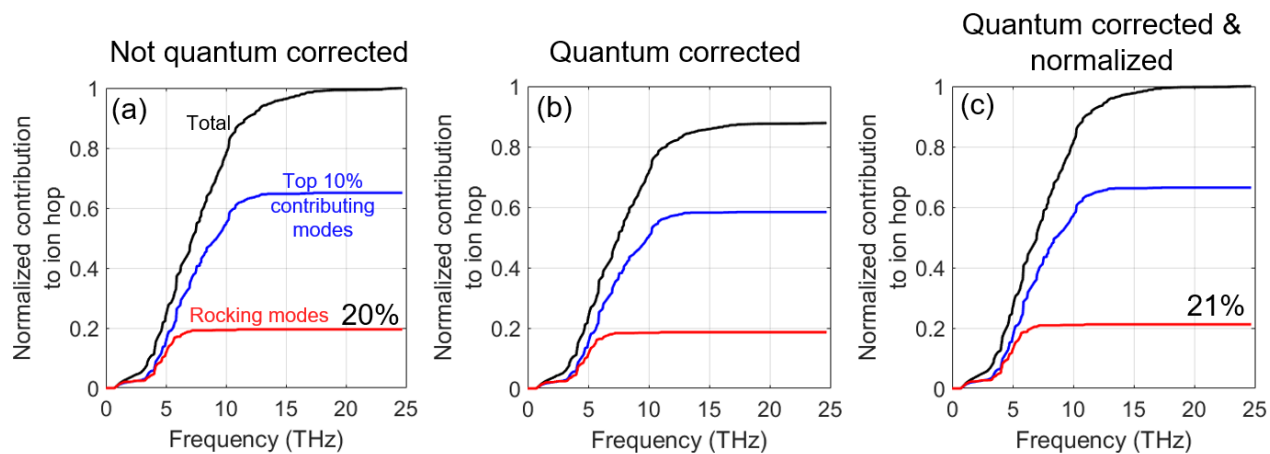


Figure S19. Effect of quantum correction on the calculated modal contributions to Li⁺ hop in the LLTO lattice. (a) The accumulative modal contributions (a) before, and (b) after quantum correction. (c) Shows the accumulative modal contributions after quantum correction, when the calculated modal contributions are normalized. It can be seen that, since most of the TiO₆ rocking modes have low frequencies (< 6THz), correcting their contribution based on Bose Einstein distribution only slightly increases their overall percentage of contribution to Li⁺ in the LLTO lattice (from 20% to 21%).

Table S4. Enhancement in the ion hopping rate by targeted excitation of the highest contributing non-rocking mode, highest contributing rocking mode, and one random mode, that have frequencies in the experimentally accessible frequency range, during MD simulations. The targeted excitation of phonons during MD simulation is explained in **Section S18** and the method is applied to three hops among the hops investigated in this study. The visualization of these hops is provided in **Fig. S20**. The numbers included in the table are ion hopping rates (#jumps/ps). Following the sorted phonon contributions shown in **Fig. S21**, almost 50% of the existing phonons in the structure do not have any noticeable contribution to the Li⁺ ion hop in the lattice, based on which, they can be categorized/labeled as “random” as opposed to their “highly contributing” counterparts.

			400 K (natural MD simulation)	700 K (natural MD simulation)	400 K (with mode excited to 700 K)
Hop #1	Jump rate (#jumps/ps)	Highest non-rocking-mode contributing mode (4.29 THz)	0.0011	1.45	1.27
		Highest rocking-mode contributing mode (3.46 THz)			1.39
		Random mode (2.66 THz)			0.0027
Hop #2	Jump rate (#jumps/ps)	Highest non-rocking-mode contributing mode (4.50 THz)	0.0024	2.07	3.61
		Highest rocking-mode contributing mode (1.84 THz)			3.23
		Random mode (3.47 THz)			0.0004

Hop #3	Jump rate (#jumps/ps)	Highest non-rocking-mode contributing mode (5.10 THz)	0.0017	1.44	2.09
		Highest rocking-mode contributing mode (1.94 THz)			1.94
		Random mode (4.43 THz)			0.0011

Figure S20. The schematic of the three hops discussed in Table S4, with structures at the beginning, during, and end of the hop displayed in both standard view (upper panel) and top view (bottom panel). The “during the hop” representation depicts the hopping atom's different positions during the hop. The bottleneck of the hop is formed by four O atoms (O-4), indicated by black lines in the “during the hop” representation, and an assisted view is provided for better visualization of the bottleneck area. The relative energies corresponding to the minimum energy pathway are displayed in the bottom-right panel.

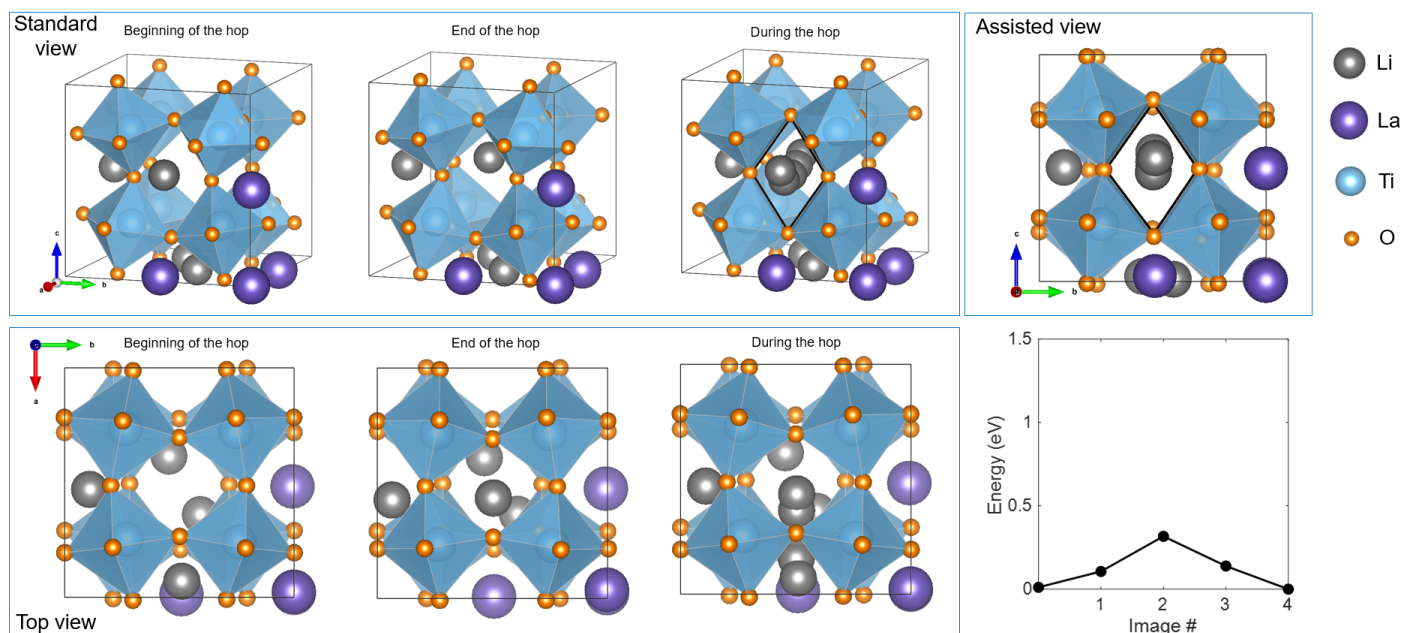


Figure S20.1. Representation of Hop #1. The shown hop is a single ion hop, and the structure is derived by repositioning of the Li atoms in the parent disordered structure #1 shown in Fig. S15.

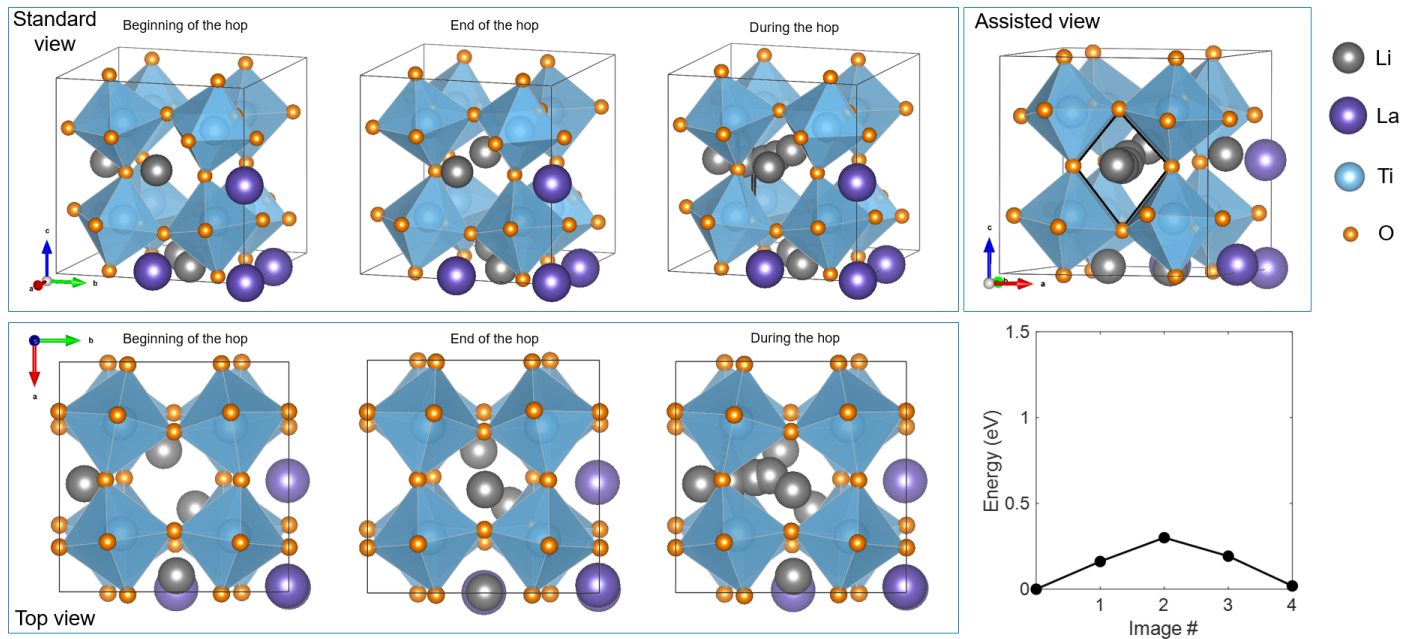


Figure S20.2. Representation of Hop #2. The shown hop is a single ion hop, and the structure is derived by repositioning of the Li atoms in the parent disordered structure #1 shown in Fig. S15.

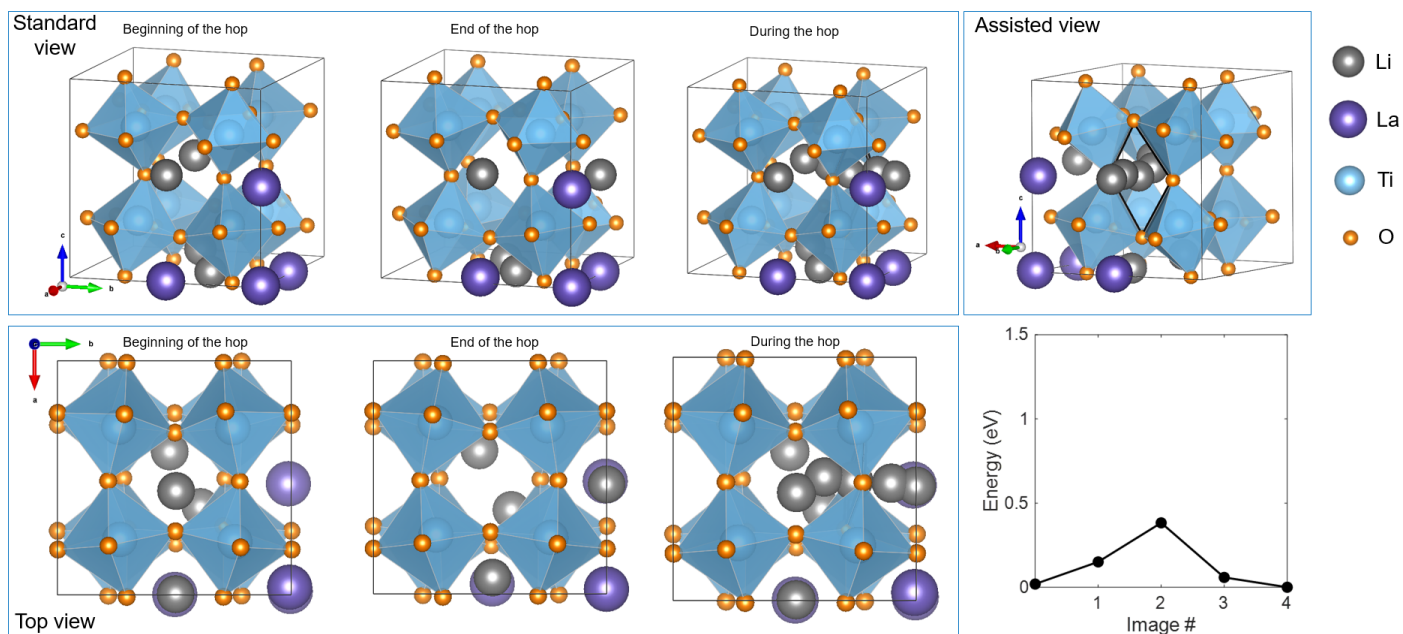


Figure S20.3. Representation of Hop #3. The shown hop is a single ion hop, and the structure is derived by repositioning of the Li atoms in the parent disordered structure #1 shown in Fig. S15.

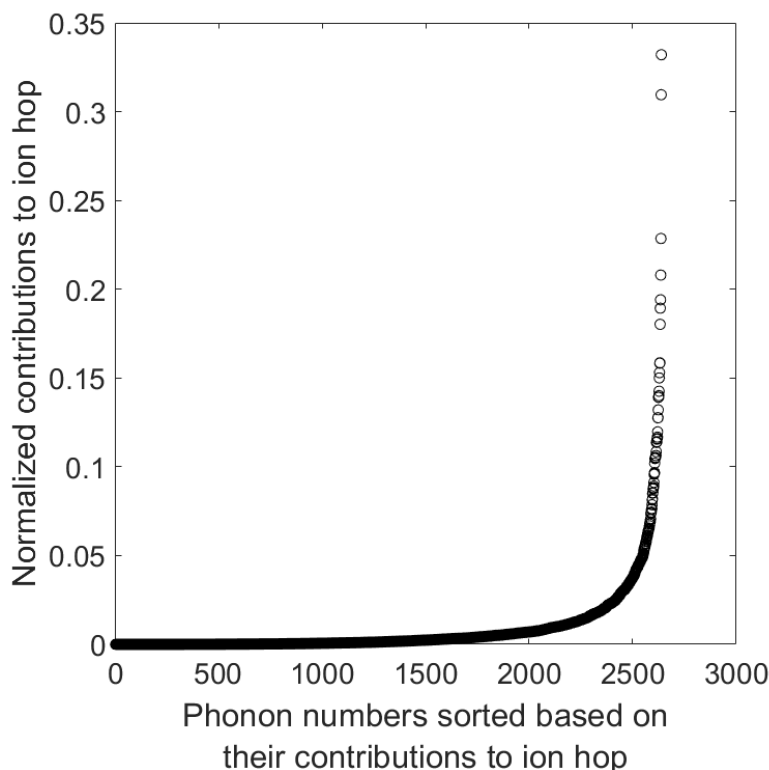


Figure S21. Sorted normalized phonon contributions to ion hop. This plot is the same as the scattered plot in Fig. S18, except that the phonons are sorted based on their normalized contributions to ion hop. The x-axis goes from 1 to 2640, which is the total number of vibrational modes that the contributions of which were investigated in this study: $(22 \text{ hops}) \times (40 \text{ atoms}) \times (3 \text{ degrees of freedom for each atom}) = 2640$.

References:

1. Inaguma, Y., Chen, L., Itoh, M. & Nakamura, T. Candidate compounds with perovskite structure for high lithium ionic conductivity. *Solid State Ion* **70**, 196–202 (1994).
2. Gallot, G., Zhang, J., McGowan, R. W., Jeon, T.-I. & Grischkowsky, D. Measurements of the THz absorption and dispersion of ZnTe and their relevance to the electro-optic detection of THz radiation. *Appl Phys Lett* **74**, 3450–3452 (1999).
3. Kresse, G. & Furthmüller, J. Efficient iterative schemes for ab initio total-energy calculations using a plane-wave basis set. *Phys Rev B* **54**, 11169 (1996).
4. Perdew, J. P., Ernzerhof, M. & Burke, K. Rationale for mixing exact exchange with density functional approximations. *J Chem Phys* **105**, 9982–9985 (1996).
5. Henkelman, G., Uberuaga, B. P. & Jónsson, H. A climbing image nudged elastic band method for finding saddle points and minimum energy paths. *J Chem Phys* **113**, 9901–9904 (2000).
6. He, X., Zhu, Y. & Mo, Y. Origin of fast ion diffusion in super-ionic conductors. *Nat Commun* **8**, 1–7 (2017).
7. Sheppard, D., Terrell, R. & Henkelman, G. Optimization methods for finding minimum energy paths. *J Chem Phys* **128**, 134106 (2008).
8. Gil-González, E., Perejón, A., Sánchez-Jiménez, P. E., Criado, J. M. & Pérez-Maqueda, L. A. Thermoanalytical Characterization Techniques for Multiferroic Materials. in *Handbook of Thermal Analysis and Calorimetry* vol. 6 643–683 (Elsevier, 2018).
9. Bohnke, O., Duroy, H., Fourquet, J.-L., Ronchetti, S. & Mazza, D. In search of the cubic phase of the Li⁺ ion-conducting perovskite La_{2/3}-xLi_{3x}TiO₃: structure and properties of quenched and in situ heated samples. *Solid State Ion* **149**, 217–226 (2002).

10. Catti, M. Short-range order and Li⁺ ion diffusion mechanisms in Li₅La₉□₂(TiO₃)₁₆ (LLTO). *Solid State Ion* **183**, 1–6 (2011).
11. Catti, M. First-Principles Modeling of Lithium Ordering in the LLTO (Li_xLa_{2/3-x/3}TiO₃) Superionic Conductor. *Chemistry of materials* **19**, 3963–3972 (2007).
12. Catti, M. Ion mobility pathways of the Li⁺ conductor Li_{0.125}La_{0.625}TiO₃ by ab initio simulations. *The Journal of Physical Chemistry C* **112**, 11068–11074 (2008).
13. Togo, A. & Tanaka, I. First principles phonon calculations in materials science. *Scr Mater* **108**, 1–5 (2015).
14. Kiarash Gordiz. ModalNEB. Preprint at <https://github.com/kgordiz/modalNEB.git> (2022).
15. Gordiz, K., Muy, S., Zeier, W. G., Shao-Horn, Y. & Henry, A. Enhancement of ion diffusion by targeted phonon excitation. *Cell Rep Phys Sci* **2**, 100431 (2021).
16. Seyf, H. R., Gordiz, K., DeAngelis, F. & Henry, A. Using Green-Kubo modal analysis (GKMA) and interface conductance modal analysis (ICMA) to study phonon transport with molecular dynamics. *J Appl Phys* **125**, 81101 (2019).
17. Dove, M. T. & Dove, M. T. *Introduction to lattice dynamics*. vol. 4 (Cambridge university press, 1993).
18. Gordiz, K. & Henry, A. Phonon transport at interfaces: Determining the correct modes of vibration. *J Appl Phys* **119**, 15101 (2016).
19. Seyf, H. R. & Henry, A. A method for distinguishing between propagons, diffusions, and locons. *J Appl Phys* **120**, 25101 (2016).
20. Gordiz, K., Singh, D. J. & Henry, A. Ensemble averaging vs. time averaging in molecular dynamics simulations of thermal conductivity. *J Appl Phys* **117**, 45104 (2015).
21. Gordiz, K. & Henry, A. Phonon transport at crystalline Si/Ge interfaces: the role of interfacial modes of vibration. *Sci Rep* **6**, 1–9 (2016).
22. Greiner, W., Neise, L. & Stöcker, H. *Thermodynamics and statistical mechanics*. (Springer Science & Business Media, 2012).
23. Du, J. & Cormack, A. N. The medium range structure of sodium silicate glasses: a molecular dynamics simulation. *J Non Cryst Solids* **349**, 66–79 (2004).
24. Cormack, A. N., Du, J. & Zeitler, T. R. Alkali ion migration mechanisms in silicate glasses probed by molecular dynamics simulations. *Physical Chemistry Chemical Physics* **4**, 3193–3197 (2002).
25. Chen, C. & Du, J. Lithium ion diffusion mechanism in lithium lanthanum titanate solid-state electrolytes from atomistic simulations. *Journal of the American Ceramic Society* **98**, 534–542 (2015).
26. Plimpton, S. Fast parallel algorithms for short-range molecular dynamics. *J Comput Phys* **117**, 1–19 (1995).
27. McGaughey, A. J. H. & Kaviany, M. Observation and description of phonon interactions in molecular dynamics simulations. *Phys Rev B* **71**, 184305 (2005).
28. Raj, A. & Eapen, J. Deducing phonon scattering from Normal Mode excitations. *Sci Rep* **9**, 1–12 (2019).
29. Zheng, X., McLaughlin, C. V., Cunningham, P. & Hayden, L. M. Organic broadband terahertz sources and sensors. *Journal of Nanoelectronics and Optoelectronics* **2**, 58–76 (2007).